CHARACTERIZATION OF HIGH DEPOSITION RATE WIRE ARC DIRECTED ENERGY DEPOSITION OF 316L STAINLESS STEEL FOR PRESSURE BOUNDARY COMPONENTS

By

Luc K. Hagen

A thesis submitted to the Faculty and the Board of Trustees of the Colorado School of Mines in partial fulfillment of the requirements for the degree of Master of Science (Metallurgical and Materials Engineering).

Golden, Colorado
Date _____

Signed: _____
Luc Hagen

Signed: _____
Dr. Jonah Klemm-Toole
Thesis Advisor

Signed: _____
Dr. Anthony Petrella
Thesis Co-Advisor

Golden, Colorado
Date _____

Signed: _____
Dr. Ivar Reimanis
Professor and Department Head
George S. Ansell Department of Metallurgical and Materials Engineering

ABSTRACT

Wire-arc directed energy deposition (WA-DED) or wire-arc additive manufacturing (WAAM) presents a novel fabrication method for construction of pressure retaining components within nuclear power plants; reducing lead times for construction of replacement parts and potentially preventing millions of dollars in losses from power plant down time. However, ASME code changes are required before WA-DED 316L can be utilized for this application. This work aims to support these code changes.

A WA-DED process parameter study was undertaken to better understand how travel speed, interpass temperature, and filler wire metal selection impact the microstructure and mechanical properties of 316L. It was found that interpass temperature and travel speed displayed no significant impact on the mechanical properties of WA-DED 316L within the parameter ranges evaluated. However, the selection of 316LSi filler wire metal resulted in an increase in yield strength, tensile strength, and ductility over 316L filler metal, likely due to solid solution strengthening and a reduction in stacking fault energy. Across conditions, heat treated samples exceeded the ASME minimums of a yield strength of 172 MPa, a tensile strength of 482 MPa, and an elongation of 43.6% for 316L at room temperature. A heat transfer model was developed to allow for prediction of the thermal history of the WA-DED process. The heat transfer model was used in conjunction with solidification models to make predictions of dendrite spacing and growth morphology showing good agreement with experimental measurements.

Further work was undertaken to understand the role of hatch spacing on lack of fusion porosity in WA-DED builds. By increasing the ratio of hatch spacing to weld bead width, lack of

fusion defects were observed in-situ using an infrared thermal camera. It was found that lack of fusion begins to form at a critical hatch spacing to bead width ratio of over 0.68. Lastly, a large-scale WA-DED 316L body was produced to gain understanding of print strategy development and part design for WA-DED. This large-scale body was separated into three distinct sections for production and surfaces were overbuilt by approximately 6.4 mm to allow for post process machining. A 323 mm (12.7 in) tall 316L representative valve body was successfully produced through WA-DED following the print strategy developed.

TABLE OF CONTENTS

LIST OF FIGURES

LIST OF TABLES

LIST OF SYMBOLS

δ – Delta ferrite

γ – Austenite

σ – Sigma phase

$vol\%$ – Volume percent

ΔT – Undercooling

ΔT_{nuc} – Nucleation undercooling

G – Temperature gradient

V – Solidification velocity

N_0 – Nucleation site density

ϕ – Fraction of equiaxed grains

n – Material dependent coefficient

Γ – Gibbs-Thomson parameter

m – Liquidus slope

R – Dendrite tip radius

k – Partition coefficient

D – Solute diffusivity

Pe – Peclet number

ξ – Stability Parameter

q – Power Density

f – Power Fraction

Q – Total Power

η – Arc Efficiency

V – Voltage

I – Current

λ_1 – Primary Dendrite Arm Spacing

λ_2 – Secondary Dendrite Arm Spacing

a – Material Constant

b – Material Constant

ACKNOWLEDGMENTS

This research is supported by the National Science Foundation with Award No. 1822144. I'd also like to thank Oak Ridge National Laboratory and the Electric Power Research Institute for providing in-kind support.

Firstly, thanks to my advisor, Dr. Jonah Klemm-Toole, for his guidance and patience during this work, for shaping my approach to research, for pushing me to perform the best work possible, and for giving me this opportunity. I also owe many thanks to my co-advisor, Dr. Anthony Petrella for his incredible support in the simulation aspects of this work and for opening my eyes to what is possible through modelling. Many thanks to my committee members, Dr. Zhenzhen Yu and Dr. Kester Clarke, as well as to Dr. Stephen Tate for their time and inputs.

I'd like to thank all the fellow students in the Center for Welding, Joining, and Coatings Research (CWJCR) for their willingness for collaboration and discussion. I'd specifically like to thank Benjamin Schneiderman for inspiring me to pursue a Master's degree.

Lastly, my friends and family deserve numerous thanks for their continued support during my graduate studies. Thank you to everybody on the Mines cross country team for the friendships and memories. Thank to you my cat, Esme, for keeping me humble, and my dog, Maybell, for keeping me active. Thank you to my sister, Ella Hagen, for always making me smile and for your unwavering belief in me. Thank you to my mother, Eva Hagen, and father, Michael Hagen, for your enduring support and counsel. Finally, thank you to my partner, Heather Keniry, for your constant inspiration and encouragement.

CHAPTER 1

INTRODUCTION

Wire-arc directed energy depositions (WA-DED), also known as wire-arc additive manufacturing (WAAM), is being considered as a potential fabrication method for pressure boundary components in nuclear power plants. Producing components through WA-DED could reduce lead time for replacement parts when failure occurs, potentially decreasing power plant down time and preventing millions of dollars in losses. However, changes to ASME code are required to use WA-DED to produce large 316L stainless steel pressure boundary components for nuclear power plants.

WA-DED systems consist of a heat source, commonly either gas metal arc welding (GMAW) or gas tungsten arc welding (GTAW) based, and a motion mechanism, which is commonly based around a robotic arm [1.1]. Compared with other additive manufacturing (AM) processes, WA-DED is particularly suited for producing components for power generation applications. WA-DED can be used to produce larger scale parts; part size is mostly limited to the reach of the WA-DED torch, whereas in process like laser powder bed fusion (LPBF) the size of parts produced is constrained by bed size. Additionally, the wire feedstock used for WA-DED is often more economical than the powder feedstock used in other AM process, and WA-DED produced parts demonstrate high density and strength. However, WA-DED does have a lower resolution that other AM methods, therefore, finishing via machining is often required [1.2]. 316L stainless steel is being considered as a possible material for power generation applications. 316L displays high corrosion resistance, high strength, high ductility, and performs well at elevated temperatures [1.3]. 316L is also a readily weldable stainless steel alloy, making it an ideal candidate for the WA-DED process [1.4].

This work aims to support changes to ASME code to allow for production of pressure boundary components with high deposition rate WA-DED of 316L stainless steel through an examination of the processing – microstructure – mechanical property relationships. Specifically, this work aims to address the following research questions:

1. What are the effects of travel speed, interpass temperature, and silicon content on the tensile properties of WA-DED 316L?
2. Can a heat transfer model, in conjunction with solidification models, be used to predict the as-built microstructure of WA-DED 316L?
3. What is the critical hatch spacing between passes to generate lack of fusion porosity, and can porosity be detected in process?
4. What considerations must be made when designing parts to be made by WA-DED?

Chapter 2 gives a literature review of the existing work in WA-DED and further background for the motivation for this work.

Chapter 3 focuses on a parameter study performed to study the effects of travel speed, interpass temperature, and wire composition. Results are qualified through microstructural evaluation and investigation mechanical properties. Additionally, this chapter presents a heat transfer model that was developed to capture the thermal history of WA-DED builds; this model, in conjunction with solidification models, is used to to make microstructure predictions of WA-DED 316L in the as-built condition.

Chapter 4 presents work done on introducing lack of fusion process defects into WA-DED 316L. By increasing hatch spacing between parallel weld beads lack of fusion is induced. Additionally, lack of fusion formation is detected in-situ with a thermal camera system.

Chapter 5 outlines the build process for a large-scale, representative, 316L valve body produced through WA-DED, focusing on print strategy, part design, and toolpath generation.

Chapter 6, through a summary of this work and results, presents answers to the key research questions asked above and proposes possible future research directions.

1.1 References

1.1 Wu, Bintao, et al. "A review of the wire arc additive manufacturing of metals: properties, defects and quality improvement." Journal of Manufacturing Processes 35 (2018): 127-139.

1.2 Frazier, William E. "Metal additive manufacturing: a review." Journal of Materials Engineering and performance 23.6 (2014): 1917-1928.

1.3 Desu, Raghuram Karthik, et al. "Mechanical properties of Austenitic Stainless Steel 304L and 316L at elevated temperatures." Journal of Materials Research and Technology 5.1 (2016): 13-20.

1.4 J.C. Lippold, V.F. Savage “Solidification of austenitic stainless steel weldments: Part I—a proposed mechanism” Weld. J., 58 (1979), pp. 362-374

CHAPTER 2

LITERATURE REVIEW AND BACKGROUND

This chapter gives a review of previous literature as it relates to WA-DED of 316L. Section 2.1 examines the structure and solidification of 316L, with a focus on solidification during welding, as it applies to the WA-DED process. Section 2.2 outlines previous studies of heat treatments effect on WA-DED. Section 2.3 focuses on process parameters and deposition rates of WA-DED process, and section 2.4, presents previous studies on defects in WA-DED.

2.1 Solidification of 316L

Solidification of stainless steels commonly follow five possible pathways, as outlined by Elmer: single-phase austenite (A), primary austenite with second-phase ferrite (AF), eutectic ferrite and eutectic austenite (E), primary ferrite with second-phase austenite (FA), and single-phase ferrite (F) [2.1]. Alloy composition plays a key role in controlling solidification mode for austenitic stainless steels. Nickel equivalent describes the combined effect of austenite stabilizing elements within the alloy. Likewise, chromium equivalent describes the combined effects of ferrite stabilizing elements. The ratio of these two terms can be used to predict primary solidification pathway. Multiple equations for nickel and chromium equivalences have been generated by researchers by comparing weld microstructures to compositions, and corresponding diagrams can be used to predict microstructure and solidification mode. These diagrams include the Shaeffler, DeLong, and the WRC 1992 [2.2][2.3][2.4]. Following these equations, it is expected that 316L solidifies as primary ferrite with secondary phase austenite (FA) mode [2.5].

Lippold provided a detailed description the FA solidification mode. Delta-ferrite (δ) is the initial phase to solidify, solidifying in a cellular dendritic form. Upon cooling, much of this

ferrite transforms to austenite (γ), which initially forms at the ferrite dendrite boundaries. In 316L, this transformation continues until a majority of the ferrite transforms, leaving ferrite only at the former dendrite cores in the form of “vermicular” or skeletal delta-ferrite. Under exposure to temperatures between 400 °C and 900 °C this retained delta-ferrite can undergo a transformation to sigma phase (σ). Sigma phase is a hard, brittle, chromium rich intermetallic phase [2.6]. The presence of sigma phase in 316L has been shown to reduce corrosion resistance [2.7], toughness [2.8], and ductility [2.9]. The control of sigma phase is therefore a key consideration for WA-DED 316L parts.

2.2 Heat Treatment of WA-DED 316L

Heat treatment present a possibly method in controlling phase distribution within WA-DED 316L. Chen *et al*. have previously studied heat treatment of WA-DED 316L. They constructed representative 316L builds before heat treating for one hour at 1000 °C, 1100 °C and 1200 °C, as well as for four hours at 1200 °C, and followed by water quenching and characterized these builds through tensile testing and microstructure examination. In the as-built condition, they observed a microstructure of primarily austenite with skeletal delta-ferrite and sigma phase, consistent with Lippold’s description of FA solidification for austenitic welds. They then calculate the volume percent (vol%) of delta-ferrite and sigma phase using SEM images, finding that the as-solidified microstructure displays both ferrite and sigma phases, with amounts of 7.84 and 4.45 vol% respectively. After a one hour heat treatment at 1000 °C a decrease in ferrite to 3.92 vol% and an increase in sigma phase to 6.98 vol% was observed. After one hour at 1100 °C no sigma phase and 5.79 vol% delta ferrite was observed, and after one hour at 1200 °C the amount of ferrite decreases to 3.96 vol%. They show that heat treatment for four hours at 1200 °C results in a completely austenitic microstructure. Large columnar grains were

observed across every condition showing little effect heat treatment on grain structure, with exception for the 1200 °C heat treatment for four hours conditions, which displayed some amount of recrystallization.

Tensile tests were then performed on each condition. Compared to the as-built condition, the 1000 °C for one hour condition shows a slight increase in yield strength (YS) and ultimate tensile strength (UTS), but a decrease in elongation. The 1100 °C for one hour displays a slight decrease in YS, and a similar UTS when compared to the as-built condition, but there was a significant increase in elongation in this condition. After heat treatment at 1200 °C for one hour a YS and UTS decrease is observed with a corresponding increase in elongation. This trend continues for the 1200 °C for four hours condition. Chen *et al.* attributes these differences across conditions to the varying amount of delta-ferrite and sigma phase [2.10].

Similar work undertaken by Rodrigues *et al.* agrees with the work done by Chen *et al.* This work indicates that heat treatment is a key step to control microstructure and phase distribution of WA-DED 316L. They show that heat treatment at 950 °C for two hours results in the formation of sigma phase in amounts near 17%, heat treatment at 1050 °C for two hours results in a microstructure free of sigma phase with approximately 3% delta ferrite, and heat treatment at 1200 °C for one hour results in a nearly completely austenitic structure [2.16]. These results, along with the work done by Chen *et al.* indicate that heat treatment is an effective tool to control the phase distribution within WA-DED 316L but has limited effect in changing grain morphology.

2.3 Process Parameters and Deposition Rate of WA-DED

Tabernero *et al*. studied the effect of welding process for WA-DED 316L, examining plasma welding (PAW), cold metal transfer (CMT) and TopTig through a comparison of tensile properties. A 1.5 kg/hr deposition rate was maintained across weld processes. They show that the TopTig process results in greater ductility and yield strength than samples produced through CMT and PAW, which show similar mechanical properties. It should be noted however, that Tabernero *et al*. found that TopTig has a much lower maximum deposition rate of 1.5 kg/hr than other processes studied, with CMT having a maximum deposition rate of 5 kg/hr and PAW showing a maximum of 3.5 kg/hr. They also note that gas selection is key to account for bead geometry. Shielding gas selection can influence bead geometry to result in a relatively wider bead, allowing for more bead overlap during the WA-DED process [2.17].

Wang *et al.* compared two arc mode for WA-DED 316L, a pulse spray weld mode and a short circuit transfer mode (ARC) with a constant wire feed rate of 4.5 m/min. The short circuit transfer mode results in a lower power and therefore heat input than the pulsed spray weld mode. They observed that the samples produced with the lower heat input short circuit transfer mode displayed a finer solidification structure, but showed no significant difference in tensile strength, yield strength, or ductility [2.18].

Rosli *et al.* have reviewed work examining the effects of heat input on the WA-DED process, covering the effects on mechanical properties and microstructure. They show that with increasing heat input, solidification rate correspondingly drops, promoting growth of columnar grains. Lowering heat input has been shown to increase the solidification rate resulting in smaller observed grain sizes; however, porosity has been shown to increase with lower heat input. Rosli.

et al. also report that structures manufactured through a GMAW based WA-DED process show little change in mechanical properties with altering heat input [2.11].

Cunningham, *et al.* have studied how heat input influences WA-DED of 316LSi by controlling both heat input and interpass temperature. They found that increasing both heat input and interpass temperature resulted in an increase in delta-ferrite within the microstructure, but that heat input had a limited effect on mechanical properties. They also show that higher interpass temperature samples show less distortion, possibly indicating a reduction in residual stresses [2.12]. These results show that heat input can influence microstructure by impacting solidification during the WA-DED process; however, heat input effects have not been shown to have significant impacts on mechanical properties of WA-DED samples. This presents an area for further study.

Overall, much of the previous work on WA-DED of 316L focuses on deposition rates in the 1-3 kg/hr range, although higher deposition rates can be achieved using two GMAW power sources and robot arms in tandem [2.19][2.20]. Bunty *et al*., in a review of the WA-DED process show the deposition rate for various WA-DED processes, as summarized in Table 2.1. Increased deposition rate has the benefit of reducing production time, presenting a key area for study.

Table 2.1 Summary of deposition rates for WA-DED [2.20].

Energy Source	Deposition Rate (kg/hr)
GMAW	3-4
GMAW-CMT	2-3
Tandem GMAW	6-8
GTAW	1-2
PAW	2-4

2.4 Influences of Process-Induced Defects on Mechanical Properties of WA-DED

Defects in WA-DED produced parts can occur due to numerous reasons including poor tool-path planning, unstable weld pools, environmental contamination, and high residual stresses. Porosity can come about because of contamination, from both the wire and atmosphere, as well as from the tool path. Complex tool paths are particularly susceptible to porosity [2.13]. Xue, *et al.* have demonstrated that mechanical properties of WA-DED produced Al-Li alloys are improved by working to control micropores that form during solidification. They demonstrate that hot-deformation successfully closes this microporosity within the WA-DED sample, leading to a UTS increase from 230 MPa to 439 MPa [2.14].

Gas pores have been induced into WA-DED Ti-6Al-4V samples by building specimens with intentionally contaminated wire feedstock. Walls were built with wire coated with WD-40® to induce the formation of pores over 100 µm in diameter. Walls built with the contaminated wire displayed a density of 99.96%, vs the 99.99% density of the control builds, with an average pore size of 200 µm in the contaminated wire builds and 60 µm for the control builds. Tensile testing of these samples shows a comparable yield strength and ultimate tensile strength between the contaminated and control samples; however, the contaminated samples display a much lower elongation, which is attributed to micro-crack formation at pore sites [2.15].

Literature shows that defects within WA-DED have critical impacts on part performance; however, there is extremely limited work done on the impacts of process defects on the mechanical properties of WA-DED 316L. Work on inducing controlled defects and studying the impact of these defects on the mechanical properties of WA-DED is a critical area of study for WA-DED 316L.

2.6 References

2.1 Elmer, J. W., S. M. Allen, and T. W. Eagar. "Microstructural development during solidification of stainless steel alloys." Metallurgical transactions A 20.10 (1989): 2117-2131.

2.2 Schaeffler, Anton L. "Constitution diagram for stainless steel weld metal." Metal progress 56.11 (1949): 680.

2.3 DeLong, W. T. "Measurement and calculation of ferrite in stainless steel weld metal." Weld. J. 21.11 (1956): 521-528.

2.4 Kotecki, D. J., and T. A. Siewert. "WRC-1992 constitution diagram for stainless steel weld metals: a modification of the WRC-1988 diagram." Welding Journal 71.5 (1992): 171-178.

2.5 Korinko, P. S., and S. H. Malene. "Considerations for the weldability of types 304L and 316L stainless steel." practical failure analysis 1.4 (2001): 61-68.

2.6 J.C. Lippold, V.F. Savage “Solidification of austenitic stainless steel weldments: Part I—a proposed mechanism” Weld. J., 58 (1979), pp. 362-374

2.7 Conejero, O., M. Palacios, and S. Rivera. "Premature corrosion failure of a 316L stainless steel plate due to the presence of sigma phase." Engineering Failure Analysis 16.3 (2009): 699-704.

2.8 Kim, Y. H., et al. "The effect of sigma phases formation depending on Cr/Ni equivalent ratio in AISI 316L weldments." Materials & Design 32.1 (2011): 330-336.

2.9 Gill, T. P. S., et al. "On microstructure-property correlation of thermally aged type 316L stainless steel weld metal." Metallurgical Transactions A 20.6 (1989): 1115-1124.

2.10 Chen, Xiaohui, et al. "Effect of heat treatment on microstructure, mechanical and corrosion properties of austenitic stainless steel 316L using arc additive manufacturing." Materials Science and Engineering: A 715 (2018): 307-314.

2.11 Rosli, Nor Ana, et al. "Review on effect of heat input for wire arc additive manufacturing process." journal of materials research and technology 11 (2021): 2127-2145.

2.12 Cunningham, C. R., et al. "Characterisation of Austenitic 316 LSi Stainless Steel Produced by Wire Arc Additive Manufacturing with Interlayer Cooling." 2019 International Solid Freeform Fabrication Symposium. University of Texas at Austin, 2019.

2.13 Wu, Bintao, et al. "A review of the wire arc additive manufacturing of metals: properties, defects and quality improvement." Journal of Manufacturing Processes 35 (2018): 127-139.

2.14 Xue, Chengpeng, et al. "Improving mechanical properties of wire arc additively manufactured AA2196 Al–Li alloy by controlling solidification defects." Additive Manufacturing 43 (2021): 102019.

2.15 Biswal, Romali, et al. "Criticality of porosity defects on the fatigue performance of wire+ arc additive manufactured titanium alloy." International Journal of Fatigue 122 (2019): 208-217.

2.16 Rodrigues, Tiago A., et al. "Effect of heat treatments on 316 stainless steel parts fabricated by wire and arc additive manufacturing: Microstructure and synchrotron X-ray diffraction analysis." Additive Manufacturing 48 (2021): 102428.

2.17 Tabernero, Paskual, Amagoia, Pedro Álvarez, and Alfredo Suárez. "Study on arc welding processes for high deposition rate additive manufacturing." Procedia Cirp 68 (2018): 358-362.

2.18 Wang, Leilei, Jiaxiang Xue, and Qiang Wang. "Correlation between arc mode, microstructure, and mechanical properties during wire arc additive manufacturing of 316L stainless steel." Materials Science and Engineering: A 751 (2019): 183-190.

2.19 Williams, Stewart W., et al. "Wire+ arc additive manufacturing." Materials science and technology 32.7 (2016): 641-647.

2.20 Tomar, Bunty, S. Shiva, and Tameshwer Nath. "A review on wire arc additive manufacturing: Processing parameters, defects, quality improvement and recent advances." Materials Today Communications (2022): 103739.

CHAPTER 3

HIGH DEPOSITION RATE WIRE-ARC DIRECTED ENERGY DEPOSITION OF 316L: PROCESS EXPLORATION AND MODELLING

Based on a paper to be submitted to the journal, *Materials Science and Engineering: A*

Luc Hagen[1], Zhenzhen Yu[1], Amy Clarke[1], Kester Clarke[1] Stephen Tate[2], Anthony Petrella[1], Jonah Klemm-Toole[1]

3.1 Abstract

A parameter design of experiments was undertaken to study the impact of wire selection, weld speed, and interpass temperature on the microstructure and mechanical properties of high deposition rate Wire-Arc Directed Energy Deposition (WA-DED) of 316L stainless steel. Small-scale, representative builds were constructed using a high deposition pulsed spray weld mode. Across conditions, WA-DED 316L builds exceeded ASME minimums for yield strength, elongation, and tensile strength at room temperature. It was found that 316LSi displayed significantly higher strength and ductility than parts produced with 316L, while the impact of weld speed and interpass temperature were less significant. A heat transfer model of the WA-DED process was created to allow for microstructure predictions. A thermal camera system was used to calibrate this model, with temperature measurements being taken from both fixed points during the build and across the solid liquid interface of the melt pool. Solidification models were developed to allow for predictions of microstructural features in the as-built condition. Predictions of dendrite spacing and growth morphology show good agreement with experiments

[1] Colorado School of Mines, Metallurgical and Materials Engineering
[2] Electric Power Research Institute (EPRI)

demonstrating the potential for modeling the influences of the WA-DED parameters for process optimization.

3.2 Introduction

The use of wire-arc directed energy deposition (WA-DED) or wire arc additive manufacturing (WAAM) is being considered as a fabrication method for pressure components within nuclear power plants. This would allow for reduced lead time for fabrication of power plant replacement parts, decreasing plant down time and potentially preventing millions of dollars in losses [3.1]. However, updates to ASME code are needed to use WA-DED to construct large 316L stainless steel pressure retaining components.

Austenitic stainless steels like 316L are ideal for power generation applications due to their combination of high corrosion resistance, strength/ductility balance, and good elevated temperature performance [3.2]. Additionally, 316L is a highly weldable stainless steel alloy, making it an ideal candidate for WA-DED [3.3]. In addition, when compared to other metal additive manufacturing methods, WA-DED allows for fabrication of larger parts, and the wire feedstock used is more economical than the powder used in other metal additive manufacturing processes. Parts produced with WA-DED show high density and good mechanical properties. However, due to the lower spatial resolution of WA-DED, finishing via machining is often required as well as a post process heat treatment [3.4].

Understanding the solidification of 316L allows for better understanding of WA-DED of 316L. Solidification of 316L follows a primary ferrite solidification pathway, where delta ferrite is the primary phase during solidification. During cooling the ferrite experiences a transformation to austenite, which initially forms at the gap between ferrite dendrites. This

transformation continues until ferrite only remains at the former dendrites cores in the form of vermicular delta-ferrite (δ) [3.3] [3.8]. Delta ferrite in austenitic steels has been shown to act as a strengthening phase [3.5].

Further, at exposure to temperatures between 400 to 900 °C, delta ferrite can transform to the intermetallic sigma phase (σ). Sigma phase is a strong, brittle, chromium rich intermetallic phase, and its presence can negatively impact ductility and corrosion resistance. Due to the large heat input and slow cooling associated with WA-DED it is expected that both delta ferrite and sigma phases will be observed in the as-built condition. Tuning the amount of these phases presents a method to improve the properties of WA-DED 316L. Chen, et al. have previously studied heat treatment of WA-DED 316L to impact the amounts of ferrite and sigma phase. Their results show that heat treatment can be used to effectively remove sigma phase from the 316L microstructure, with a corresponding drop in YS and UTS and an increase in ductility [3.7].

Microstructure and part performance of WA-DED 316L has also been shown to be affected by heat input. Heat input and interpass temperature has been previously shown to impact residual stresses and mechanical performance, with heat input being shown to have impacts on grain structure and size [3.17] [3.18] [3.19]. Additionally, ferrite and sigma phase formation, along with dendrite spacing, is directly influenced by solidification and cooling rates [3.3] [3.5] [3.20]. Understanding this process, structure, properties, and performance (PSPP) relationship will allow for production of better performing WA-DED 316L part. Additionally, much of the previous work with WA-DED of stainless steel focuses on deposition rates ranging from 1 to 3 kg/hr [3.27] [3.28]. However, higher deposition rates could allow for increased productivity and shorter build times.

In this study, we seek to better understand the PSPP relationship for WA-DED 316L through a systematic study of processing parameters and wire feedstock composition. The influence of various heat treatments on WA-DED 316L is characterized to select a viable heat treatment used for a parametric study of the impacts of travel speed, interpass temperature, and wire selection between 316L and 316LSi. Additionally, a finite element analysis (FEA) heat transfer model was developed to understand the thermal history experienced by WA-DED builds. Analytical solidification models were also applied so that in combination with heat transfer simulations, the microstructure in the WA-DED builds could be predicted.

3.3 Experimental Methods

The following sections outline the experimental methods followed.

3.3.1 Build Parameters and Wire Filler Metal Compositions

To construct builds, a Lincoln Electric S500 Power Wave gas metal arc welding (GMAW) power source with a RapidX pulsed spray weld mode was used. For the wire feedstock, Lincoln Electric Blue Max® MIG 316L with a 1.14 mm (0.045 in) diameter was used with a feed rate of 10.16 m/min (400 in/min), resulting in a deposition rate of approximately 5 kg/hr. Table 3.1 shows the composition of this wire. A 95% Ar + 5% CO_2 shielding gas with a flow rate of 25 CFH was used during deposition. Builds were also constructed with 316LSi filler metal, using Lincoln Electric Red Max® MIG 316LSi with a 1.14 mm (0.045 in) diameter. This composition is shown in Table 3.1. To study the impact of heat treatment on WA-DED 316L small scale, single bead, thin wall builds measuring 12.7 cm x 10.2 cm x 0.9 cm (5 in x 4 in x 0.35 in) were constructed using 316L filler metal.

Table 3.1 Typical wire composition of Lincoln Electric Blue Max® MIG 316L [3.10] and Lincoln Electric Red Max® MIG 316LSi [3.12]

	%C	%Cr	%Cu	%Mn	%Mo	%N	%Nb	%Ni	%P	%S	%Si
Lincoln Electric Blue Max® MIG 316L	0.01 -0.02	18.5 -18.7	0.03 -0.13	1.6 - 1.8	2.1 - 2.6	0.03	0.01 max.	11.8 - 12.2	0.02	0.01 max	0.39 - 0.40
Lincoln Electric Red Max® MIG 316LSi	0.01-0.02	18.2-18.3	0.07-0.10	1.7	2.3	0.06 - 0.07	0.01 max.	11.3	0.02	0.02	0.79 – 0.87

3.3.2 Experimental Methods: Processing Parameter Experimental Design

A full factorial design was undertaken to study the impacts of travel speed, interpass temperature, and wire composition. Small scale builds were constructed with a size of 22.9 cm x 11.5 cm x 1.14 cm (9 in x 4.5 in x 0.45 in). To generate builds with increased width, the GMAW torch path was weaved, as outlined in Table 3.2. Weave parameters changed with build parameter to keep the bead width at a constant 1.14 cm (0.45 in) across build conditions. Build parameters for this parameter experiment are presented in Table 3.3.

Table 3.2 Weave parameters for DOE builds

Material	Travel Speed	Weave Velocity	Weave Amplitude
316L	50.8 cm/min (20 in/min)	134.6 cm/min (53 in/min)	0.69 cm (0.27 in)
316L	63.5 cm/min (25 in/min)	198.2 cm/min (78 in/min)	0.76 cm (0.30 in)
316LSi	50.8 cm/min (20 in/min)	114.3 cm/min (45 in/min)	0.53 cm (0.21 in)
316LSi	63.5 cm/min (25 in/min)	165.1 cm/min (65 in/min)	0.71 cm (0.28 in)

Table 3.3 Build conditions for parameter study

`Build	Material	Travel Speed	Interpass Temperature
1	316L	50.8 cm/min (20 in/min)	350 °C
2	316L	63.5 cm/min (25 in/min)	350 °C
3	316L	50.8 cm/min (20 in/min)	100 °C
4	316L	63.5 cm/min (25 in/min)	100 °C
5	316LSi	50.8 cm/min (20 in/min)	350 °C
6	316LSi	63.5 cm/min (25 in/min)	350 °C
7	316LSi	50.8 cm/min (20 in/min)	100 °C
8	316LSi	63.5 cm/min (25 in/min)	100 °C

The high and low levels for this build parameter were dictated by the usable window for build construction. At travel speeds lower than 50.8 cm/min (20 in/min), molten metal in the builds would sag. At speeds higher 63.5 cm/min (25 in/min), the track welding system could not weave at the necessary velocity to maintain a 1.14 cm (0.45 in) build width. The 350 °C temperature was based on the highest interpass temperature that could be consistently controlled with the system used for these builds, while the 100 °C interpass temperature was set as the lowest temperature at which the cooling time was reasonable for build construction.

3.3.3 Experimental Methods: Post-Build Heat Treatment

To study heat treatment, builds using parameter set #1 from Table 3.3 were heat treated at 900 °C, 1040 °C, and 1200 °C for one hour in air using a Carbolite CWF 13/5 furnace and then immediately water quenched. These results were used to select a heat treatment regime for the parametric study.

3.3.4 Experimental Methods: Tensile Testing

For the post-build heat treatment study, subsized, round tensile bars were machined from the heat-treated builds, oriented parallel to the build direction, and tensile tested in accordance with to ASTM E8 [3.11]. Following construction of the processing conditions shown in Table 3.3, each build was sectioned, with a portion being left in the as-built condition and a portion being heat treated at 1040 °C for one hour and water quenched. Builds were than machined as outlined in Figure 3.1(b). From each build 10 tensile bars were cut out, 5 in the build direction and 5 in the transverse direction, with 1 tensile bar in each direction from the as-built condition and 4 tensile bars from the heat-treated condition. Flat tensile specimens were machined in accordance with ASTM E8, tensile bar geometry is shown in Figure 3.1(a) [3.11]

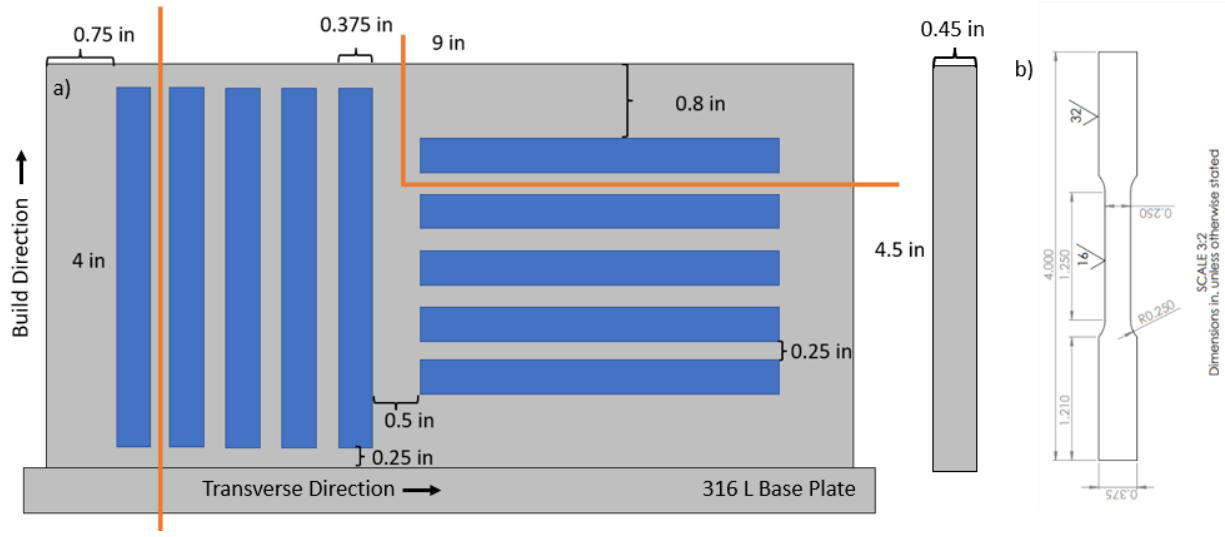

Figure 3.1 (a) Schematic of builds used for the parametric study showing tensile bar layout and sectioning. Sectioning lines are marked in orange and indicate the portion of the build that was left in the as-built condition. b) Drawing of the ASTM E8 specimen machined from the builds.

Tensile testing was performed at a strain rate of $1x10^{-3}$ s^{-1} on an MTS Landmark 22.5 kip load frame in accordance to ASTM E8 [3.11] For the post-build heat treatment study, two tensile tests were performed for each condition at room temperature. For the builds generated in the parametric study in the heat-treated condition, two tensile tests were performed from each direction at room temperature. In the as-built condition, one tensile test was performed in both the build direction and transverse direction at room temperature. An additional two samples in the heat-treated condition from each direction were tensile tested at 427 °C (800 °F) based on ASME code requirements. Samples tested at elevated temperatures were heated using a thermocouple-controlled induction heater. Thermocouples were welded to samples prior to testing.

3.3.5 Experimental Methods: Microstructure Characterization

Metallographic specimens were sectioned from each condition and polished to a final step of 0.05 µm diamond or colloidal silica. Electron backscatter diffraction (EBSD) using a JEOL 7000F field-emission scanning electron microscope (SEM) operating at 20 kV with a 15 mm working distance was performed to analyze the microstructure and phase distribution of the builds. Grain structure was examined by etching polished specimens with a Beraha 1 reagent, made up of 100 ml deionized water, 20 ml HCL, 2.4 g NH_4FHF, and 0.6 g $K_2S_2O_5$, to capture grain boundaries [3.35]. A glyceregia etchant, composed of 15 ml HCL, 10 ml Glycerol, and 5 ml of HNO_3, was used to capture dendrite structures [3.36]. Etched micrographs were taken using an Olympus DSX500 optical microscope. Grain size measurements were made from images collected from samples etched with the Beraha 1 reagent. Due to the columnar nature of the grains observed, grain width was calculated for grain size measurements. Grain width was calculated by overlaying horizontal lines across each micrograph and totaling the number of

grain boundaries intersected by these lines using ImageJ software. The line distance was then divided by the number of grain boundaries to give an average grain width. Dendrite arm spacing was measured from images etched with the glyceregia etchant.

3.3.6 Experimental Methods: Heat Transfer Model of WAAM Process

Development of the Abaqus heat transfer model described was performed by Dr. Anthony Petrella. The single bead, thin wall WA-DED builds were modeled in the commercial finite element software, Abaqus (v.2021). The familiar 3D heat conduction equation was solved using a transient heat transfer simulation and mass transfer was modeled using the built-in element activation features of Abaqus/Standard. Convection within the molten pool was neglected. The latent heat of fusion was not modeled explicitly, but the heat required for phase transformation was considered by defining specific heat as a function of temperature through the solidus-liquidus transition [3.37] [3.38]. Thermal conductivity [3.38] [3.39] and density [3.37] were also temperature dependent.

Convection and radiation boundary conditions were prescribed on the top and side surfaces of the substrate and evolving free surfaces of the build volume. The bottom surface of the substrate was treated as insulated. The reference (i.e., far-field ambient) temperature for the purpose of convection and radiation boundary conditions was defined as 26°C. The convection coefficient was $36*10^3$ (mW/mm^2 °C). The emissivity ratio was 0.28[3.39].

Heat input was modeled by a moving source with a double ellipsoid power density distribution defined by Goldak and Akhlaghi, shown in equation 3.1 and 3.2 [3.40].

$$q_{(f/r)} = \frac{6\sqrt{3}f_{(f/r)}Q}{a_{(f/r)}bc\pi\sqrt{\pi}} exp\left[\frac{-3x^2}{a_{(f/r)}^2}\right] exp\left[\frac{-3y^2}{b^2}\right] exp\left[\frac{-3z^2}{c^2}\right] \quad (3.1)$$

$$f_f + f_r = 2 \tag{3.2}$$

Where q is power density (mW/mm^3) and mutually exclusive subscripts f and r refer to front or rear halves of the double ellipsoid, respectively. The dimension a (mm) was measured along the length of the power density distribution, which was aligned with the local x-axis and parallel to the path of the moving heat source. Dimensions b and c (mm) defined the width and depth of the power density field, respectively. Parameter f was the power fraction, the values of which in the front and rear regions of the power distribution must obey equation 3.2 [3.40]. Values of f_f and f_r in the present study were defined by the following relations:

$$f_f = 2\left(\frac{a_f}{a_f + a_r}\right) \tag{3.3}$$

$$f_r = 2\left(\frac{a_r}{a_f + a_r}\right) \tag{3.4}$$

Total power input Q (mW) was defined by,

$$Q = \eta \times V \times I \tag{3.5}$$

where η is arc efficiency, V (V) is voltage, and I (mA) is current for the WA-DED process. Parameters a, b, and c, were estimated from visual inspection of the experimental conditions and all heat source parameters are summarized in Table 3.4.

Table 3.4 Heat source parameters for the WA-DED simulation performed in Abaqus.

Parameter	a_f (mm)	a_r (mm)	b (mm)	c (mm)	f_f	f_r	η	V (V)	I (mA)
Value	5.3	10.6	4.6	2.34	0.67	1.33	0.85	22	0.210

For simplicity, the arc path was modeled as a straight line in the heat transfer simulation. Nodal temperature data were extracted from the melt pool region within the fourth (top) layer of the WA-DED deposition and these data were used for later computation of thermal gradient, solidification velocity, and cooling rate. Time histories of nodal temperature were also extracted for fixed points on the lateral surface of the simulated build volume for validation comparison with experimental measurements. The setup of the model is illustrated in Figure 3.2.

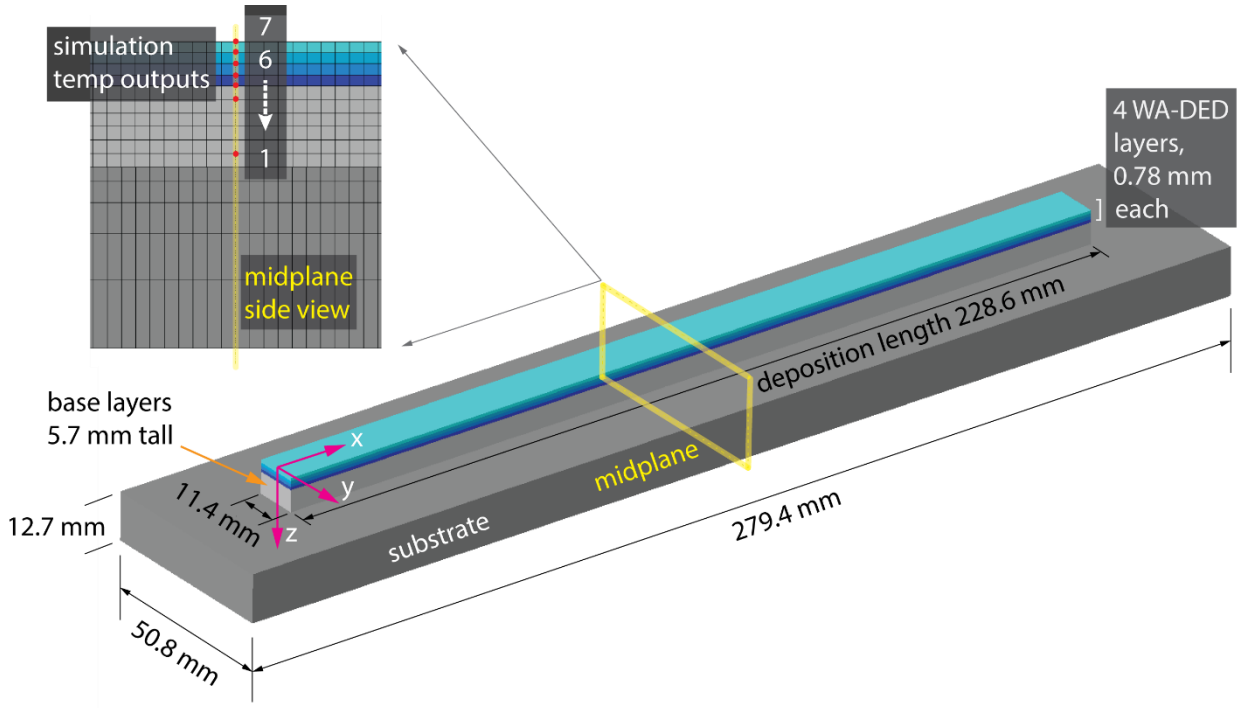

Figure 3.2 Set up for heat transfer model, showing arc path as well as location from which nodal temperature information was extracted.

A Xiris XIR-1800 short wavelength infrared thermal camera was used to measure temperatures during WA-DED to calibrate heat transfer simulations. Video capture was done from a sideview with a focal distance of 400 mm. Emissivity was set to 0.9 based on work done

by Valiorgue et al. [3.34]. Additional thermal images were taken to capture the top of the build to record melt pool shape.

3.3.7 Experimental Methods: Microstructure Development Models

The Kurz, Giovanola, Trivedi (KGT) dendrite growth model was used to predict the solidification structure in the WA-DED builds [3.22]. The model's simplified form, assuming constant solute diffusivities, partitioning coefficients, and liquidus slopes, can be solved analytically using equations 3.6 – 3.12.

$$4\pi^2\Gamma\left(\frac{1}{R^2}\right) + \left(2\sum[m_i Pe_i(1-k_i)C_i^*\xi_i]\right)\left(\frac{1}{R}\right) + G = 0 \tag{3.6}$$

$$\xi_i = 1 - \frac{2k_i}{\sqrt{1+\left(\frac{2\pi}{Pe_i}\right)^2} - 1 + 2k_i} \tag{3.7}$$

$$Pe_i = \frac{RV}{2D_i} \tag{3.8}$$

$$C_i^* = \frac{C_o}{1-[(1-k_i)Iv(Pe_i)]} \tag{3.9}$$

$$\Delta T_{c,i} = m_i(C_o - C_i^*) \tag{3.10}$$

$$\Delta T_r = \frac{2\Gamma}{R} \tag{3.11}$$

$$\Delta T_{total} = \sum_i \Delta T_{c,i} + \Delta T_r \tag{3.12}$$

Where Γ is the Gibbs-Thomson coefficient, R is the dendrite tip radius, m is the liquidus slope, k is the partition coefficient, D is the interdiffusion coefficient of a given solute in the liquid, Pe is the Peclet number, C_0 is the initial alloy composition, G is the temperature gradient within the liquid, ΔT is liquid undercooling, ξ is a stability parameter, and Iv is the Ivanstov function. To solve these models a few key material values are needed. Gibbs-Thomson coefficient, Γ, liquid diffusivity, D_i, partition coefficient, k_i, and liquidus slope, m_i. Gibbs-Thomson coefficient and liquid diffusivity values were found in literature, while partition

coefficient and liquidus slope values were determined using ThermoCalc© 2021a using the TCFE11 database based on measured compositions of the builds (Table 3.9). This model was developed to reflect six primary solutes within the alloy: Cr, Ni, Mo, Mn, Si, C.

To predict primary dendrite arm spacing (PDAS), the model proposed by Kurz was used, where the dendrite is represented as an ellipsoid with major axis, *a*, and minor axis, *b*. The dendrite tip is modelled to follow kinematics as described by a simplified LGK model [3.22] [3.26] [3.29] [3.30]. Equation 3.16, giving PDAS for multicomponent alloys, is used. In this equation, *R* as a function of *V* is taken from the KGT model developed earlier, and tip temperature is found by subtracting total undercooling from the KGT model from the liquidus temperature.

$$a = \frac{T_{tip} - T_{base}}{G} \tag{3.13}$$

$$R_{tip} = \frac{b^2}{a} \tag{3.14}$$

$$\lambda_1 = \sqrt{\frac{3R\left(T_{tip} - T_{base}\right)}{G}} \tag{3.15}$$

$$\lambda_1 = \sqrt{\frac{3(\alpha_1 V^{\beta_1})(\Delta T_o' - \alpha_2 V^{\beta_2})}{G}} \tag{3.16}$$

Where V is tip velocity, R is the dendrite tip radius, T_{tip} is the temperature at the dendrite tip, T_{base} is the temperature at the dendrite base, $\Delta T_0'$ is the freezing range of the alloy, and λ_1 is primary dendrite arm spacing. α_1 and β_1 are taken from a power law fit of a R vs V plot from the KGT model, and α_2 and β_2 are from a power law fit of total undercooling vs velocity also from the KGT model.

A similar process can be done for secondary dendrite arm spacing (SDAS). SDAS spacing evolves throughout solidification due to coarsening. A model for multicomponent

systems from Easton *et al* is used [3.9]. C_f is defined as the final composition of the liquid. Using ThermoCalc© a Scheil simulation can be performed to find $\Delta T'_0$, which is assumed to be the freezing range of the alloy.

$$\lambda_2 = 5.5\left(\frac{M\Delta T_o'}{GV}\right)^{\frac{1}{3}} \quad M = \frac{-\Gamma}{\Sigma\frac{m_i(1-k_i)(c_{f,i}-c_{o,i})}{D_i}}\ln\left[\frac{\Sigma\frac{m_i(1-k_i)c_{f,i}}{D_i}}{\Sigma\frac{m_i(1-k_i)c_{o,i}}{D_i}}\right] \tag{3.17}$$

A columnar to equiaxed transition (CET) model was then developed following the Gäumann modification to the original Hunt model [3.21] [3.31]. This modification assumes that all nucleation sites activate once liquid undercooling reached a critical undercooling for nucleation, ΔT_{nuc}. With this, thermal gradient, G, can be calculated as a function of undercooling, ΔT, as shown in equation 3.18. Nucleation site density, N_0, was estimated based on experimental measurements of grain size because it cannot be physically measured.

$$G = \frac{1}{n+1}\sqrt[3]{\frac{-4\pi N_o}{3ln[1-\emptyset]}}\Delta T\left(1-\frac{\Delta T_{nuc}^{n+1}}{\Delta T^{n+1}}\right) \tag{3.18}$$

$$\Delta T_{total} = (aV)^{\frac{1}{n}} \tag{3.19}$$

$$N_0 \sim \frac{1}{\sqrt[3]{grain\ size}} \tag{3.20}$$

Here $\emptyset$ is the volume fraction of equiaxed grains, and a and n are material dependent constants found from the undercooling vs velocity plot generated with the KGT model. A power law is fit to this plot, shown in equation 3.21. From this, a and n are calculated with equation 3.22 and 3.23. Values for these solidification models can be found in the supplemental materials section.

$$y = wx^z \tag{3.21}$$

$$n = 1/w \tag{3.22}$$

$$a = w^z \tag{3.23}$$

3.4 Results

The following sections outline the results from this study.

3.4.1 Results: Selection of Post Build Heat Treatment

Figure 3.3 illustrates the EBSD inverse pole figures (IPF) and phase maps from heat-treated builds. Each condition displays large, columnar grains typically associated with WA-DED [3.7] [3.13] [3.19] with no obvious change in grain structure across conditions. However, the amount of sigma and delta phases present varies with heat treatment. In the as-built condition, austenite grains are displayed with skeletal delta ferrite dendrite cores and sigma phase. Upon heat treatment at 900 °C much of the delta-ferrite transforms to sigma phase. Heat treatment at 1040 °C is effective in dissolving the sigma phase, resulting in a microstructure nearly free of sigma. Lastly, the sample heat treated at 1200 °C shows a completely austenitic microstructure. Table 3.5 shows the phase fractions for each condition.

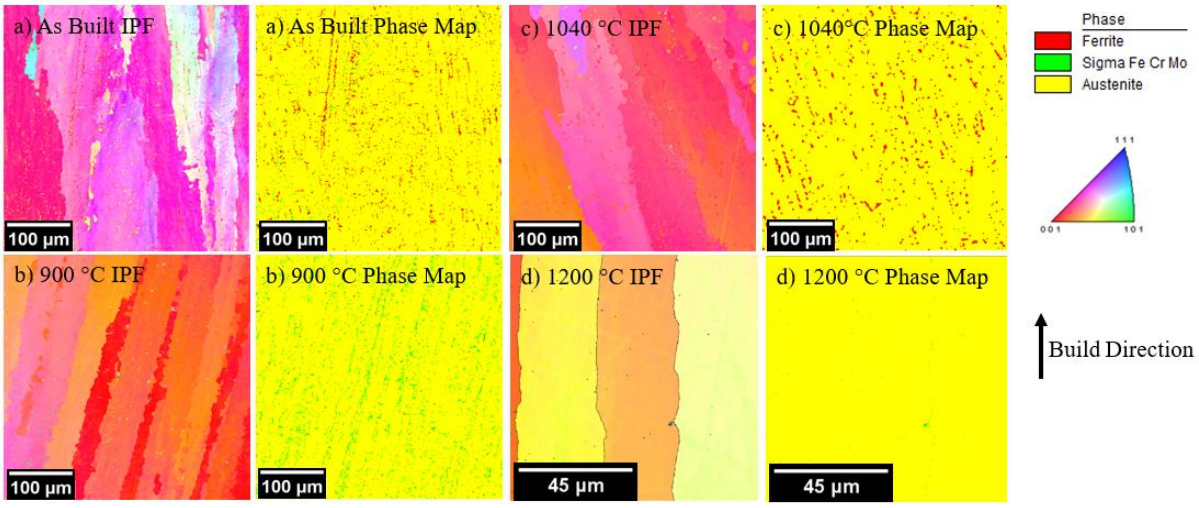

Figure 3.3 EBSD IPF and phase maps of a) the as-built condition and after heat treatment for 1 hour and water quenching at b) 900 °C c) 1040 °C d) and 1200 °C. The IPF map is oriented to the build direction.

Table 3.5 Phase amount in volume % of the as-built condition and after heat treatment for 1 hour and water quenching at 900 °C, 1040 °C and 1200 °C.

Condition	Austenite	Ferrite	Sigma
As-built	95.7	3.6	0.7
900 °C	95.1	0.1	4.8
1040 °C	96.3	3.6	0.1
1200 °C	99.9	0	0.1

The yield strength (YS), ultimate tensile strength (UTS), and reduction in area for the heat-treated builds are given in Table 3.6. Of the heat-treated conditions, 900 °C showed the highest tensile strength, but lowest ductility. This is attributed to the increased amount of sigma phase in this condition. At 1040 °C, there is a reduction in tensile strength and an increase in ductility when compared to the 900 °C condition. This is likely due to the near elimination of brittle sigma phase within the specimen. Yield strength is similar between these conditions. The as-built condition and the 1040 °C condition show similar amounts of ferrite, but the 1040 °C displayed higher ductility, likely due to the reduced amount of sigma phase. The increase in ductility from the as-built condition to the 1040 °C condition may also be a result of annealing. Heat treatment in ranges of 1000 °C to 1100 °C has been shown to relieve residual stresses and increase ductility in laser melted 316L [3.16] but further study is required to understand the stress relief mechanisms for WA-DED 316L. The 1200 °C conditions showed a near completely austenite structure, corresponding to the high reduction in area displayed in this condition. This condition also displayed the lowest YS and UTS of all conditions. This is attributed to a greater degree of annealing as well as the lack of ferrite to act as a strengthening phase in this condition [3.5].

Table 3.6 Tensile strength, yield strength, and percent reduction in area for heat treated builds.

	Tensile Strength (MPa)	Yield Strength (MPa)	Reduction in area (%)
As-built 1	541	301	59
As-built 2	503	306	45
900 1	582	272	60
900 2	596	273	50
1040 1	499	278	78
1040 2	510	268	78
1200 1	489	242	75
1200 2	479	248	77

From these results, the 1040 °C heat treatment was selected to be used for the parametric study. The 1040 °C heat treat provided a significant increase in ductility over the as-built and 900 °C conditions while maintaining high yield and tensile strengths.

3.4.2 Results: Parameter Design of Experiments – Mechanical Properties

Figure 3.4 shows tensile strength, yield strength, and percent elongation for conditions tested in the parametric study along with ASME minimums for 316L. The heat-treated specimens successfully meet ASME minimums for 316L across conditions, while the as-built specimens fail to meet elongation requirements as outlined by ASME [3.15]. This increase in ductility is in line with the results from heat treatment builds and indicates that heat treatment is a vital step for WA-DED 316L to meet performance requirements.

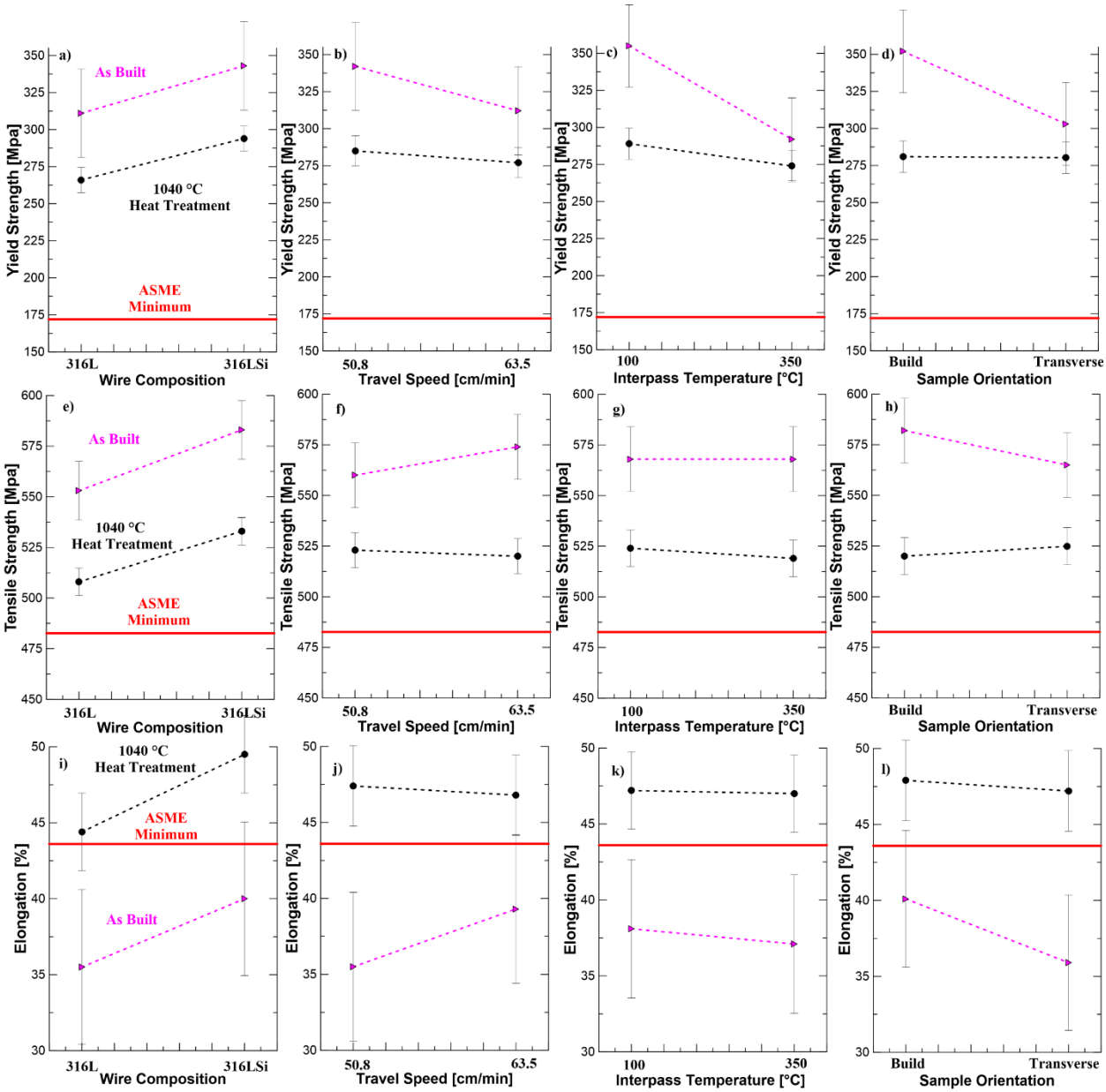

Figure 3.4 Tensile strength, yield strength, and percent elongation for parameter study builds in comparison with ASME minimums for 316L [14]. Elongation has been converted from 40% elongation in 2 in. gauge length using ISO 2566 [15].

In the as-built condition 316LSi demonstrates a performance increase over 316L, showing higher UTS, YS, and ductility. The high travel speed condition, low interpass condition, and build direction orientation showed increases in yield strength, but further testing is needed to

verify the statistical significance of these increases. Travel speed, interpass temperature, and sample orientation showed no significant influence on ductility and tensile strength.

In the heat-treated condition, like the as-built condition, selecting 316LSi wire over 316L resulted in a statistically significant increase in YS, UTS, and ductility. However, after heat treatment, weld speed and interpass temperature did not demonstrate a statistically significant effect on mechanical properties. This contrasts with the as-built, possibly indicating that after heat treatment much of effect of heat input parameters, such as weld speed and interpass temperature, is eliminated.

Figure 3.5 summarizes the tensile properties of samples tested at 427 °C (800 °F) in comparison to ASME minimums. Samples successfully exceeded minimums for YS but did not meet UTS requirements. At 427 °C the only statistically significant impact was silicon content on UTS, no other factors were shown to have a statistically significant impact on YS, UTS, or elongation.

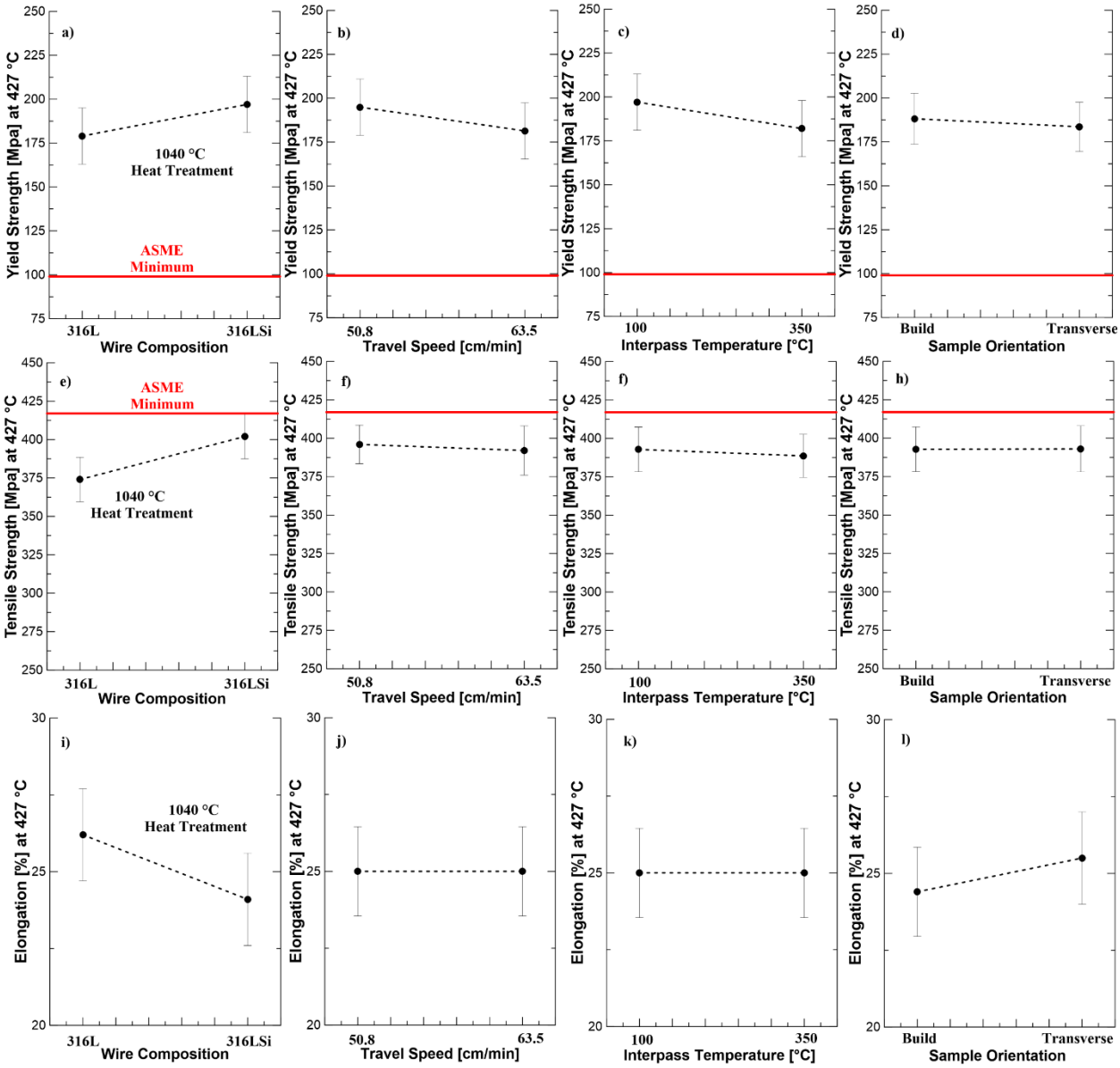

Figure 3.5 Tensile strength, yield strength, and percent elongation for parameter study builds at 427 °C (800 °F) [14].

3.4.3 Results: Parameter Design of Experiments – Microstructure Characterization

To better understand the increase in strength associated with the 316LSi wire composition, a grain size comparison between heat treated 316L and 316LSi was undertaken. Due to the columnar nature of the grains, grain width was measured from etched micrographs of representative samples (Fig 3.6), Table 3.7 summarizes these results. There is not statistically

significant difference between the grain size of 316L and 316LSi in the as-built condition. Furthermore, the grain size is not significantly altered by the post-built heat treatment. It can therefore by assumed that there is a negligible difference in grain size between all the conditions evaluated in this study.

Table 3.7 Grain width measurements (mean ± 95% confidence interval)

Condition	Average Grain Width (mm)
316L – As-built	0.34 ± 0.07
316LSi – As-built	0.33 ± 0.03
316LSi – 1040 °C Heat Treatment	0.31 ± 0.08

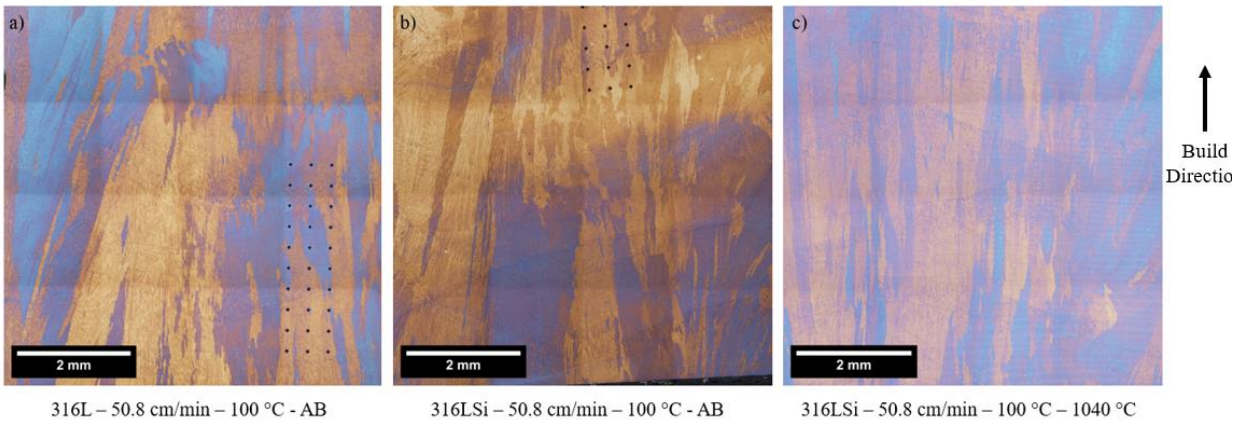

Figure 3.6 Light optical micrographs after etching of a) 316L – 50.8 cm/min travel speed - 100 °C interpass temperature – as-built condition b) 316L – 50.8 cm/min travel speed - 100 °C interpass temperature – as-built condition c) 316L – 63.5 cm/min travel speed - 100 °C interpass temperature – 1040 °C condition used for grain width measurements.

To assess the influence of solidification conditions on the microstructure, dendrite spacing measurements were made from each condition (Fig 3.7), these results are summarized in Table 3.8. No statistically significant differences in primary or secondary dendrite arms spacings were measured between the conditions evaluated.

Table 3.8 Dendrite arm spacing measurements from parameter DOE (mean ± 95% confidence interval)

Condition	Average PDAS (μm)	Average SDAS (μm)
316L –63.5 cm/min – 100 °C - As-built	25.9 ± 5.1	8.1 ± 1.6
316L –63.5 cm/min – 350 °C - As-built	23.2 ± 5.2	8.9 ± 2.1
316L – 50.8 cm/min – 100 °C – As-built	22.8 ± 5.0	8.6 ± 2.4
316L – 50.8 cm/min – 350 °C – As-built	23.7 ± 4.8	9.1 ± 1.8
316LSi – 63.5 cm/min – 100 °C – As-built	23.0 ± 5.6	8.8 ± 2.1
316LSi – 63.5 cm/min – 350 °C – As-built	23.6 ± 4.1	8.3 ± 1.7
316LSi – 50.8 cm/min – 100 °C – As-built	24.7 ± 4.1	8.4 ± 1.4
316LSi – 50.8 cm/min – 350 °C – As-built	22.3 ± 4.2	8.0 ± 1.9

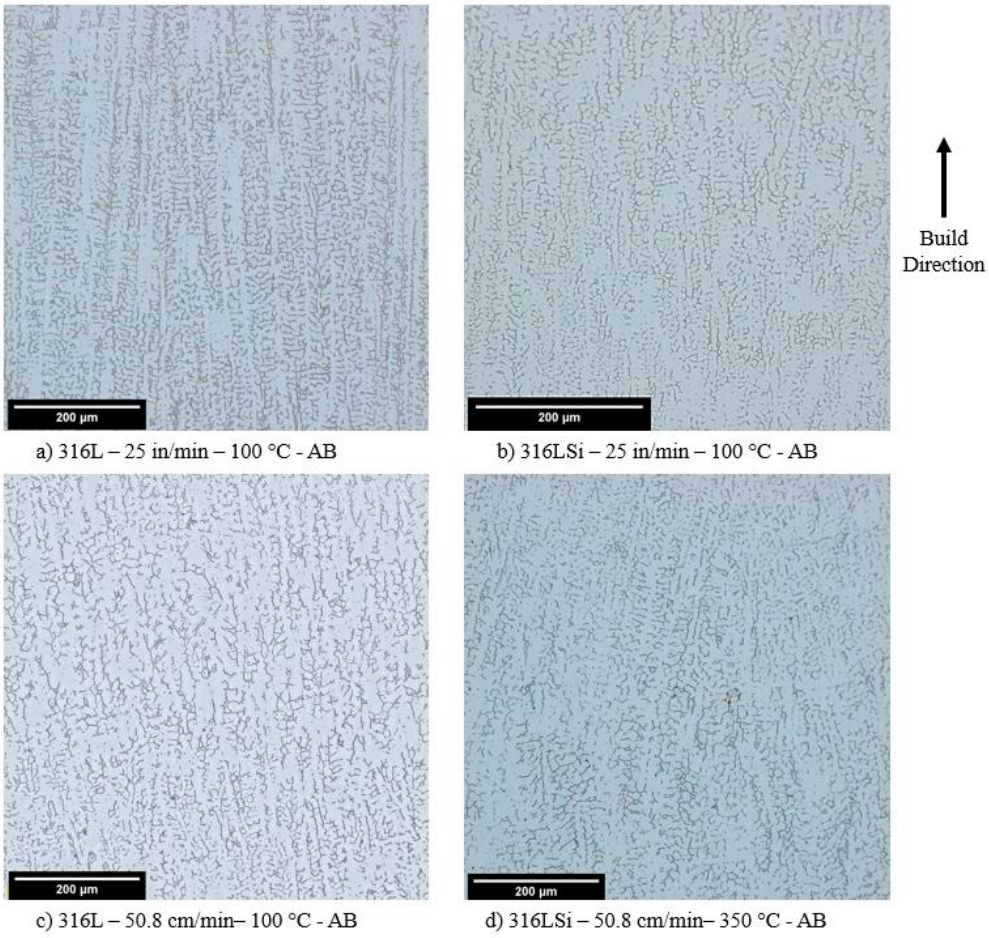

a) 316L – 25 in/min – 100 °C - AB
b) 316LSi – 25 in/min – 100 °C - AB
c) 316L – 50.8 cm/min– 100 °C - AB
d) 316LSi – 50.8 cm/min– 350 °C - AB

Figure 3.7 Light optical micrographs after etching of a) 316L – 63.5 cm/min travel speed - 100 °C interpass temperature – as-built condition b) 316LSi – 63.5 cm/min travel speed - 100 °C interpass temperature – as-built condition c) 316L – 50.8 cm/min travel speed - 100 °C interpass temperature – as-built condition d) 316LSi – 50.8 cm/min travel speed - 350 °C interpass temperature – as-built condition used for dendrite spacing measurements.

Additionally, composition analysis was performed on both 316L and 316LSi WA-DED samples using both an optical emission spectrometer and LECO Combustion units, these results are shown in Table 3.9. This compositional information is used for solidification model development.

Table 3.9 Composition measurements of 316L and 316LSi WA-DED builds (weight %)

Element	316L	316LSi
Iron	Base	Base
Chromium	18.50	18.30
Nickel	12.10	11.01
Molybdenum	2.29	2.18
Silicon	0.35	0.84
Manganese	1.71	1.57
Sulfur	0.015	0.024
Phosphorus	0.021	0.025
Carbon	0.014	0.017
Nitrogen	0.043	0.072
Oxygen	0.055	0.038

3.4.4 Results: Parameter Design of Experiments – Temperature Measurements of the Build Process

A thermal camera video was recorded to capture temperature during deposition of four consecutive layers for heat transfer model calibration. All temperature information was captured using 316L wire and corresponding weave parameter from Table 3.3. Video was recorded for a 63.5 cm/min travel speed, 30 second interpass time; a 50.8 cm/min, 30 second interpass time; and a 63.5 cm/min, 3 minute interpass time. A 30 second interpass time corresponds roughly with the 350 °C interpass temperature, while a 3 minute time corresponds with a 100 °C interpass temperature. Point temperature information was recorded as shown in Figure 3.8. Addition video was captured of the top of the melt pool to determine melt pool shape and temperature fields (Fig. 3.8).

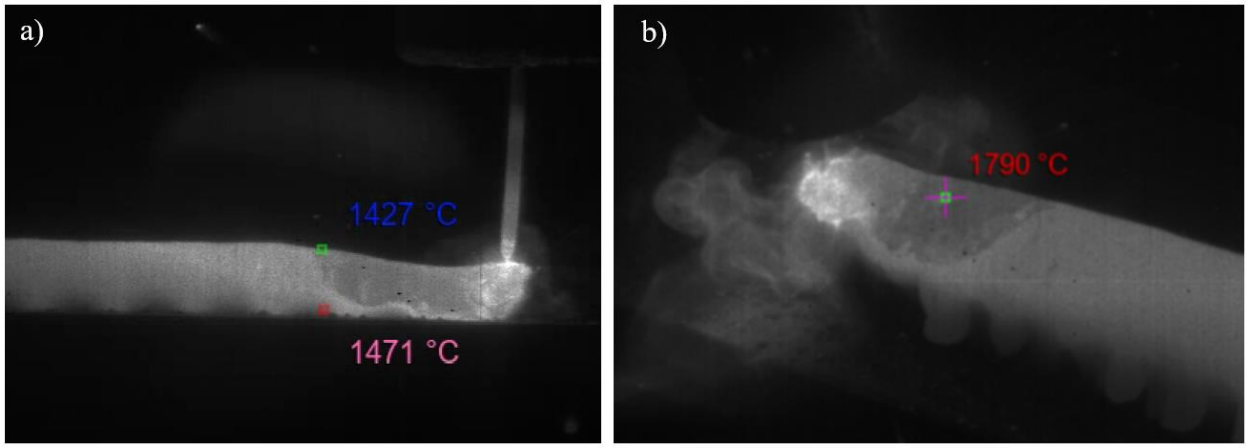

Figure 3.8. a) Side view during deposition of 316L, 63.5 cm/min travel speed condition. Point temperature measurements are taken from approximately center of build and aligned with the top and bottom of the first layer recorded. b) Top of melt pool during deposition of 316L, 63.5 cm/min travel speed condition.

3.5 Discussion

The following section describes the implications from the results described above.

3.5.1 Discussion: Microstructure Predictions of the WA-DED Process

The heat transfer model was calibrated with temperature data captured from thermal camera video. Figure 3.9 shows recorded temperature measurements from points shown in Figure 3.8a, in comparison with predicted temperature from the thermal model for four deposition passes. In the initial passes the model predicts a cooling rate slower than that measured, as can be seen by comparing the slopes of the temperature vs time curves. Subsequent passes show better agreement between the model and experiment. FEA curve 1 corresponds to the experimental point 1 while FEA curve 4 corresponds to experimental point 2. The discrepancy with FEA point 1 is likely due to latent heat not being considered within the thermal model. It may also be due to convection not being considered within the melt pool, leading to a shallower modeled melt pool then the experimental melt pool.

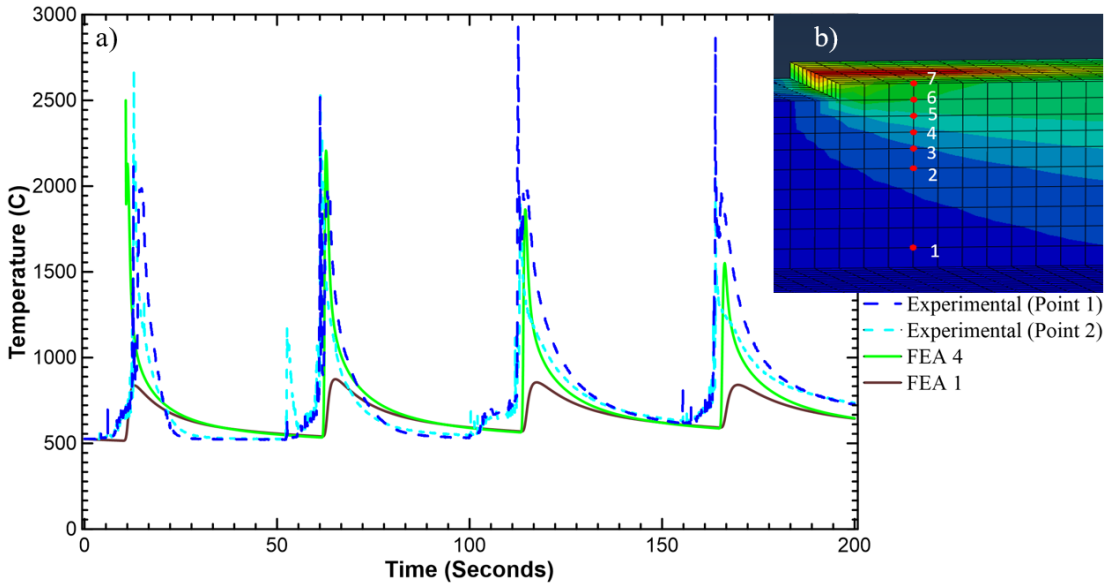

Figure 3.9 Experimental temperature vs predicted temperature showing strong agreement in cooling rates and temperature after initial passes. Experimental (Point 1) and Experimental (Point 2) are temperature measurements taken with the thermal camera corresponding with the top (Point 2) and bottom (Point 1) of the initial melt pool deposited, seen in Figure 3.8a. FEA 1 and 4 correspond to model temperature predictions for points outlined in Figure 3.9b.

For the heat transfer model, the melt pool boundary was defined with a 1440 °C isosurface, which is approximately the liquidus temperature of 316L determined from ThermoCalc©. Comparing the observed melt pool with the melt pool shape predicted by the model (Fig. 3.10), in addition to comparing cooling rates shown in Fig. 3.9 was used for model calibration. With the melt pool defined, velocity vectors and thermal gradient vectors are calculated along the melt pool surface to determine thermal gradient, *G*, and cooling rate, *C*. Solidification velocity, *V*, can then be determined using the relationship $V=C/G$. Figure 3.11 shows these vectors along the 1440 °C isosurface.

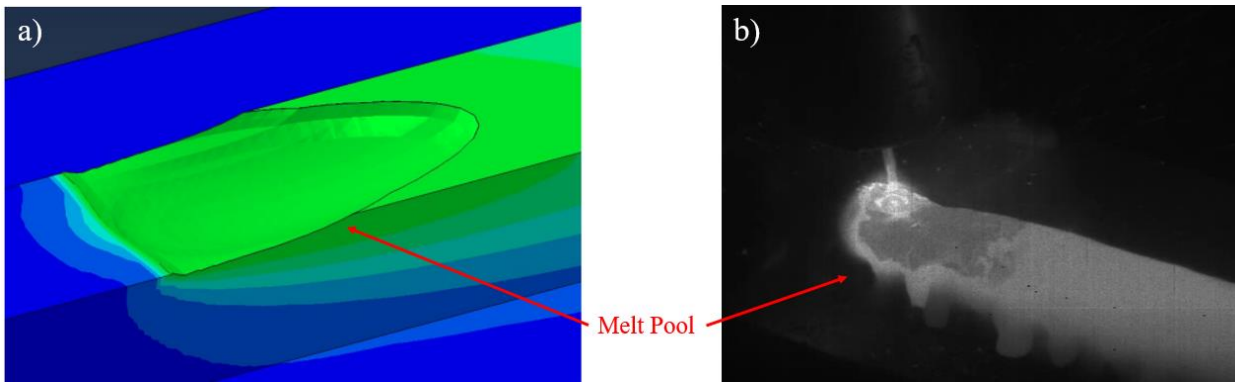

Figure 3.10 Melt pool shape as predicted by heat transfer model in comparison with experimentally observed melt pool

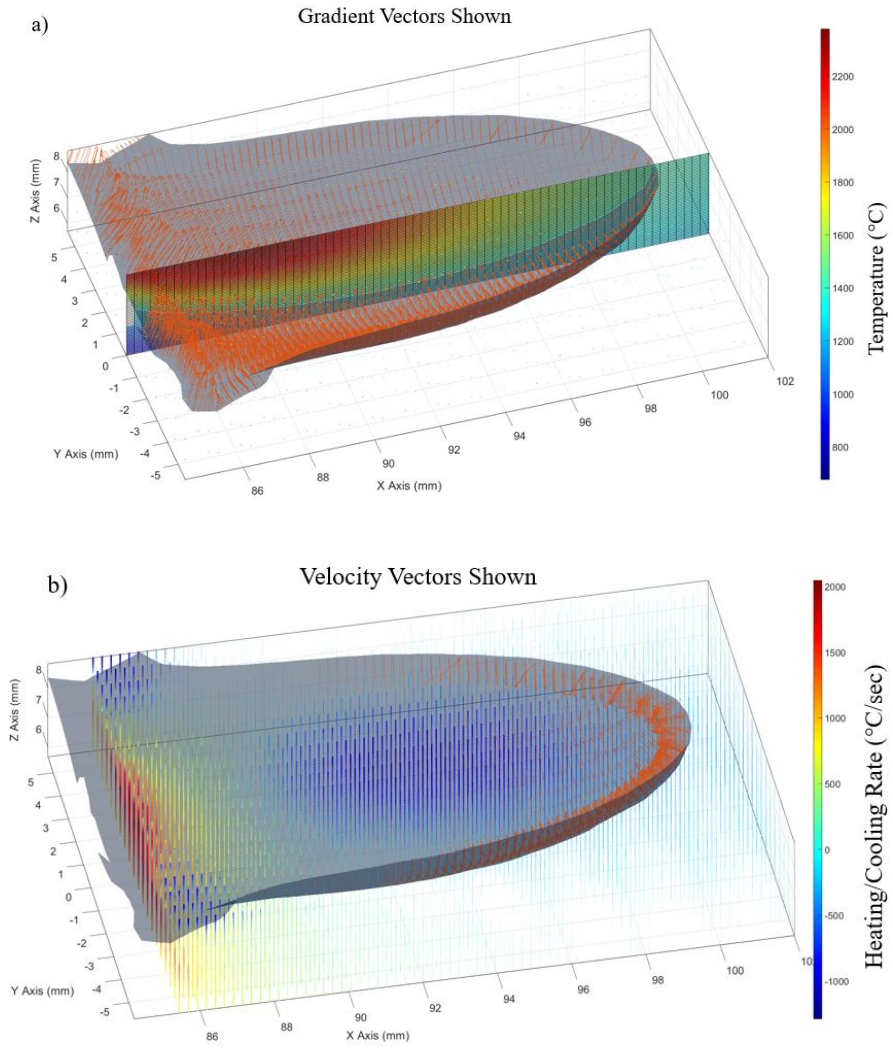

Figure 3.11 a) 1440 °C isosurface showing temperature gradient vectors. b) 1440 °C isosurface showing velocity vectors.

Temperature gradient and solidification velocity for points at the solid liquid interface were then be predicted for all thermal conditions: 63.5 cm/min travel speed, high interpass temperature; 50.8 cm/min travel speed, high interpass temperature; 63.5 cm/min travel speed, low interpass temperature; and 50.8 cm/min travel speed, low interpass temperature. The heat transfer model predicts a minimal change in G and V across conditions, as shown in Figure 3.12.

Dendrite arm spacings were then be modelled using Equations 3.6 – 3.23, measured compositions of the builds listed in Table 3.9, and G, V predictions from heat transfer model results to allow for microstructure predictions. Detailed values from the microstructure prediction models are shown in Supplemental Materials section (Table 3.12 – 3.17). Experimental dendrite arm spacings were measured from the center of the build towards the bottom of each melt pool, as shown in Figure 3.13. Measurements near the top of the melt pool are remelted in subsequent passes, so no microstructural measurements were made from these regions. All model prediction shown are for 316L in Figure 3.12, but negligible differences in model predictions or measurements were found between 316L and 316LSi, as shown in Figure 3.15 in the supplemental materials section. Measured values of PDAS and SDAS are shows as a single point in Figure 3.12. Dendrite growth morphology predictions from the CET model are also shown in Figure 3.12. A near completely columnar microstructure is predicted, consistent with what is observed in experimental microstructures.

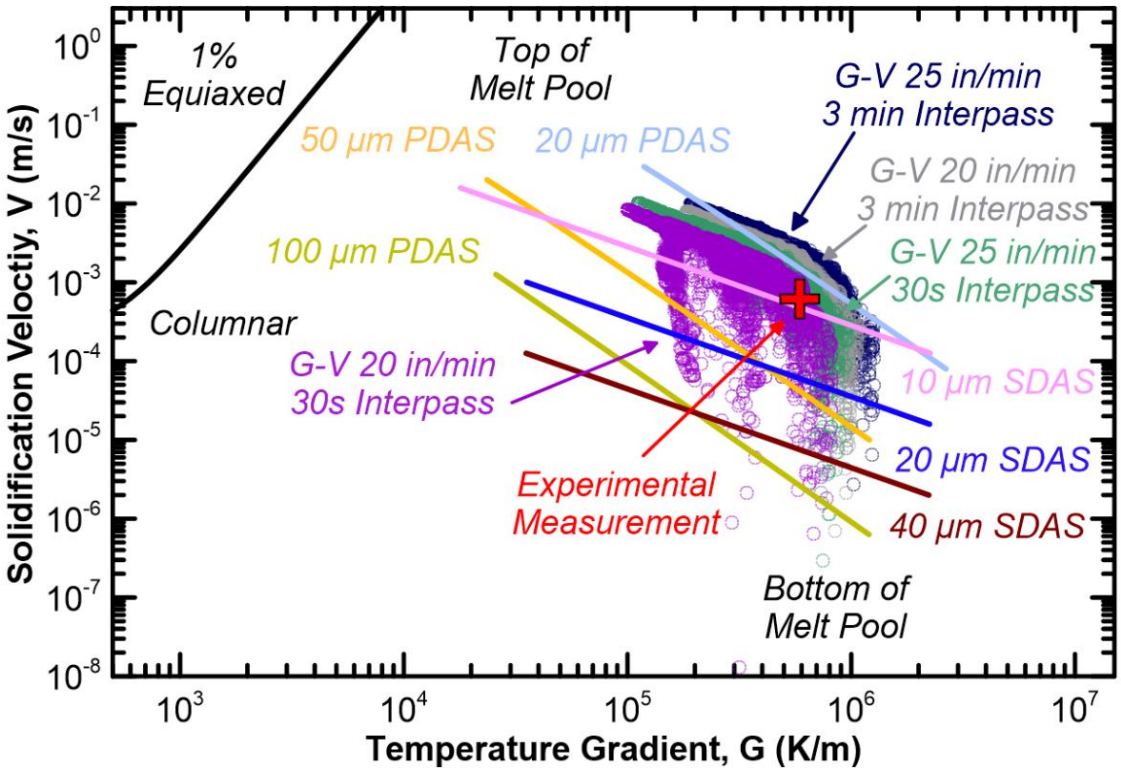

Figure 3.12 *G,V* values from heat transfer model with predicted dendrite arm spacings for 316L in comparison with experimentally measured dendrite arm spacings. Experimental measurement point combines both PDAS and SDAS

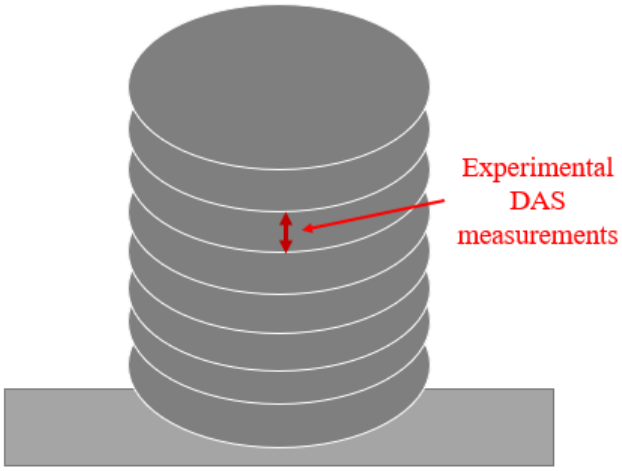

Figure 3.13 Diagram showing area of melt pool that was not remelting during deposition of subsequent layers, from which dendrite arm spacing measurements could be made.

With model predictions from each condition, predicted values can be compared to experiments. G-V values for the middle of the melt pool, corresponding with the highest thermal

gradient, are given in Table 3.10. Additionally, Table 3.10 also shows the predicted PDAS and SDAS for each condition as well as the experimental measurements. In general, the confidence intervals of PDAS and SDAS measurements contain the simulation results, suggesting good agreement. The PDAS and SDAS measurements are predicted to decrease with increasing travel speed and decreasing interpass temperature, however there is not a statistically significant difference in measurements between the conditions evaluated. Error in experimental measurements may have arisen from taking dendrite arm spacing measurements from locations not exactly at the center of the melt pools. However, relatively small changes in spacing (less than 4 μm) are predicted within the conditions evaluated. Overall, the combination of heat transfer simulations of WA-DED and solidification models for 316L allowed for microstructure predictions of the as-built condition that are in reasonable agreement experimental results showing the potential for predicting the influences of processing parameters for process optimization and design.

Table 3.10 Predicted G-V and PDAS-SDAS from the middle of the melt pool and experimental DAS measurements.

Condition (As-built)	G (K/m)	V (m/s)	PDAS Predicted (μm)	SDAS Predicted (μm)	PDAS Experimental (μm)	SDAS Experimental (μm)
316L – 50.8 cm/min – 350 °C	$5.8*10^{5}$	$9.7*10^{-4}$	22.5	7.9	23.7± 4.8	9.1 ± 2.1
316L –63.5 cm/min – 350 °C	$6.4*10^{5}$	$1.2*10^{-3}$	20.3	7.2	23.2± 5.2	8.9 ± 2.1
316L – 50.8 cm/min – 100 °C	$6.1*10^{5}$	$1.9*10^{-3}$	19.1	6.3	22.8 ± 5.0	8.6 ± 2.4
316L –63.5 cm/min – 100 °C	$6.4*10^{5}$	$1.9*10^{-3}$	18.0	6.2	25.9 ± 5.1	8.1 ± 1.8

3.5.2 Discussion: Influences of Si on Mechanical Properties

The increase in strength the 316LSi samples over 316L samples is likely not a result of microstructure differences because statistically insignificant changes between grain size and dendrite spacing was observed across samples. It is possible that the added silicon acts as a solid solution strengthener. Eliasson and Sandström have previously shown that at room temperature, silicon strengthens austenitic stainless steels with a factor of 23 MPa/wt.% Si [3.25]. From the composition analysis, the 316LSi samples contain approximately 0.49 wt.% more silicon than the 316L samples leading to an expected increase in yield strength of 11.3 MPa. The 316LSi filler wire used in this study contained 0.03 wt% more nitrogen than the 316L filler wire. Eliasson and Sandström have shown that N is a potent solid solution strengthener, with an expected strengthening factor of over 800 MPa/wt.% N [3.25]. The resulting expected increase in yield strength from nitrogen solid solution strengthening would be approximately 24 MPa. At room temperature, in the heat-treated condition, an increase in yield strength of 28 ± 10 MPa was observed in 316LSi compared to 316L. The measured difference in yield strength is slightly lower than the expected difference in solid solution strengthening from silicon and nitrogen of 35.3 MPa, but within the margin of error. It is possible that unaccounted for differences in other element concentrations between 316LSi and 316L lead to lower-than-expected differences in strength.

Eliasson and Sandström also show the solid solution strengthening effect of silicon and nitrogen decrease with increasing temperature. At 427 °C they predict a strengthening factor of approximately 7 MPa/wt.% Si and 400 Mpa/wt.% N [3.25]. After testing at 427 °C, the 316L Si samples in this work display a smaller yield strength increases of 18 MPa greater than 316L

samples, albeit statistically insignificant. Further study is needed to understand the greater strengthening effect of silicon observed in WA-DED of 316L.

The increase in ductility observed in 316LSi samples is likely not a result of solid solution strengthening. Fig. 3.14 shows engineering and true stress strain curves of one 316L and one 316LSi sample both built with a 50.8 cm/min travel speed, a 350 °C interpass temperature, and from the transverse direction. The engineering stress strain curves show that the major difference in ductility between the 316L and 316LSi samples is uniform elongation. Table 3.11 shows values of uniform and post-unform elongation for 316L and 316LSi are shown in Table 3.11 confirms that the greater ductility in 316LSi is primarily due to a higher uniform elongation. From the true stress strain curve shown in Figure 3.14, after yielding the 316L sample initially displays a higher strain hardening rate compared to the 316LSi sample. However, the 316LSi sample maintains a higher strain hardening rate to higher strains leading to the greater uniform elongation that the 316LSi condition exhibits. Previous literature has shown that addition of silicon to austenitic stainless steels and reduction in Ni content lowers stacking fault energy, 316LSi samples showed approximately 1 wt.% less Ni then 316L samples [3.23] [3.24]. It is likely that the addition of silicon and reduction of nickel lowers the stacking fault energy of WA-DED 316L specimens, suppressing cross slip and delaying dynamic recovery to larger strains, which results in a higher uniform elongation.

Table 3.11 Uniform and post-uniform elongation for 316L and 316LSi wire compositions.

	% Total Elongation	% Uniform Elongation	% Post Uniform Elongation
316LSi Average	49.5	34.5	15.0
316L Average	44.4	30.2	14.2

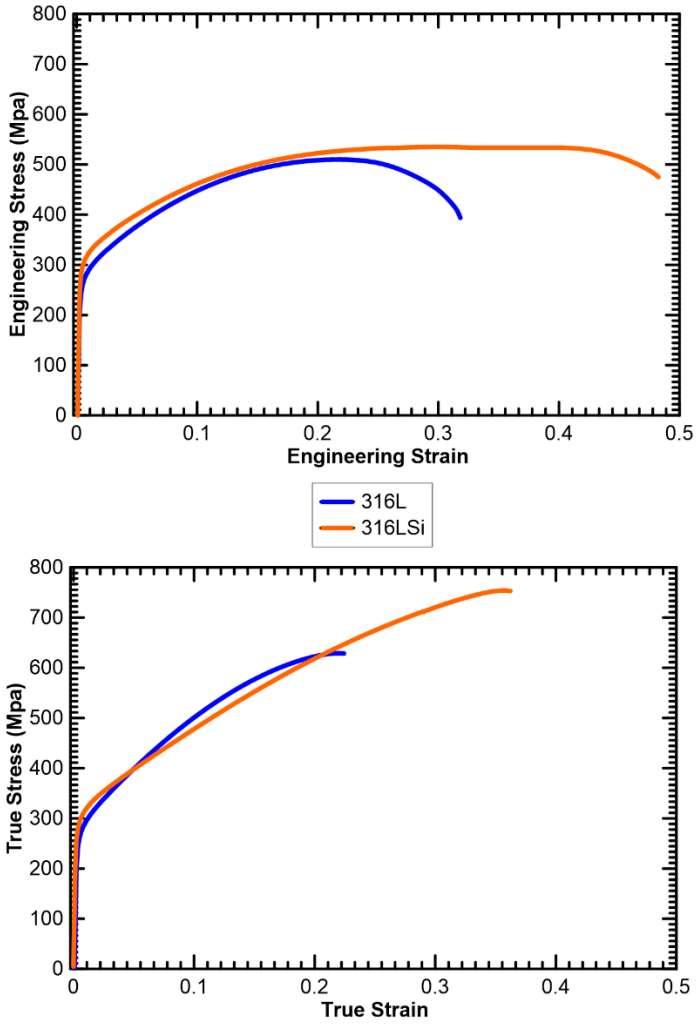

Figure 3.14 Engineering and True stress and strain for 316L and 316LSi specimens from the transverse direction built with a 50.8 cm/min travel speed and a 350 °C interpass temperature

3.5.3 Discussion: Elevated Temperature Performance

At 427 °C (800 °F) samples from the parametric study exceeded minimums for yield strength but failed to meet ASME minimums for tensile strength. The low values of ultimate tensile strength in WA-DED samples may be attributed to the large grain size relative to the specimen size. Previous work has shown that a large grain size in comparison to the tensile specimen geometry can lower strain hardening rates, possibly leading to the failure to meet UTS minimums at 427 °C [3.32]. Further work is needed to validate WA-DED 316L for high

temperature applications; elevated temperature tensile testing with larger tensile specimens can be used to evaluate any changes in strain hardening. It is interesting to note that due to the large grain size observed, WA-DED 316L is expected to have good creep performance, as the large grains minimize the potential for grain boundary sliding [3.33]. This presents another opportunity for future study of WA-DED 316L.

3.5.4 Discussion: Influence of Travel Speed, Interpass Temperature, and Sample Orientation

From the parametric study, interpass temperature and travel speed showed minimal influence on the mechanical properties and microstructure in the heat-treated condition. Changing these processing parameters resulted in no significant change in grain size, dendrite spacing, yield strength, tensile strength, or ductility. High deposition rate WA-DED, as studied here, has a limited processing window where shape accuracy during the building process can be maintained. Changes to travel speed and interpass temperature within this operating range are likely not large enough to significantly impact mechanical properties and microstructure. Additionally, sample orientation showed minimal effect on mechanical properties, despite the strongly oriented columnar grains observed. This may be due to a limited number of grains being captured within the tensile specimens as well as the small boundary strengthening component in the microstructure.

3.6 Conclusions

The microstructure and mechanical properties of high deposition rate WA-DED of 316L were investigated using a combination of experiments and models. From the results described here, the following conclusions are made:

- Heat treatment is an effective way in tuning the phase distribution of the printed material, but has little effect on grain morphology. The as-built condition showed large, columnar austenite grains with skeletal ferrite and a small amount of sigma phase, with heat treatments at temperatures ranging from 900 °C to 1200 °C altering the phase fractions present. A heat treatment of 1040 °C for one hour and water quenching was selected for use in a parameter effect study. This heat treatment resulted in a near elimination of brittle sigma phase, increasing ductility from the as-built condition while maintaining high strength.
- After heat treatment at 1040 °C, specimens from a parametric study examining travel speed, interpass temperature, and wire composition successfully met ASME minimums for 316L at room temperature; however, specimens from the as-built condition failed to meet minimum ductility requirements.
- Travel speed and interpass temperature had minimal impact on mechanical properties, but the 316LSi wire composition displayed significantly increased ductility, yield strength, and tensile strength over 316L wire. The increase in strength is likely a result of solid solution strengthening from the added silicon and nitrogen, although strengthening observed in this work exceed values reported previously in austenitic stainless steels. The increased ductility observed in this work is attributed to the lowering stacking fault energy of added silicon and reduced nickel.
- At 427 °C (800 °F) specimens met ASME minimums for yield strength but failed to meet tensile strength requirements. The lower-than-expected tensile strengths measured in this work is possibly due to the large grain size relative to the tensile specimens utilized.

- A heat transfer model was successfully developed to predict the thermal history of WA-DED builds. Predictions from the heat transfer model in combination and dendrite arm spacing and morphology models were in agreement with experimental measurements demonstrating the possibility of modeling the effects of WA-DED process parameters to aid in process design and optimization.

3.7 Supplemental Materials

Table 3.12 Values used for KGT model for 316L

Solute	D (m^2/s)	k (unitless)	m (K/wt%)	C_0 (wt %)
Cr	$1.90*10^{-9}$	1.06	4.65	18.5
Ni	$1.90*10^{-9}$	0.734	-3.91	12.1
Mo	$1.90*10^{-9}$	1.18	4.76	2.29
Mn	$1.90*10^{-9}$	0.7489	-1.76	1.71
Si	$1.90*10^{-9}$	0.7	-2.7	0.35
C	$1.90*10^{-8}$	0.11	-127.4	0.014

Table 3.13 Values used for KGT model for 316L

Γ	$2.60*10^{-7}$
T_L (°C)	1446
T_S (°C)	1333

Table 3.14 Values used for KGT model for 316LSi

Solute	D (m^2/s)	k (unitless)	m (K/wt%)	C_0 (wt %)
Cr	1.90E-09	1.04	1.146	18.3
Ni	1.90E-09	0.734	-6.345	11.01
Mo	1.90E-09	1.16	1.75	2.18
Mn	1.90E-09	0.741	-4.54	1.57
Si	1.90E-09	0.739	-5.52	0.84
C	1.90E-08	0.118	-122.7	0.017

Table 3.15 Values used for KGT model for 316LSi

Γ	$2.60*10^{-7}$
T_L (°C)	1450
T_S (°C)	1318

Table 3.16 Values used for CET and DAS Models for 316L

N0 (1/m^3)	$9.80*10^{11}$
ΔT_n (K)	2.5
a	$3.305*10^{3}$
n	3.425
ϕ (%)	1
Ts (°C)	1333
T_L (°C)	1446

Table 3.17 Values used for CET and DAS Models for 316LSi

N0 (1/m^3)	$9.80*10^{11}$
ΔT_n (K)	0.1
a	$3.425*10^{3}$
n	3.305
ϕ (%)	1
Ts (°C)	1450
T_L (°C)	1318

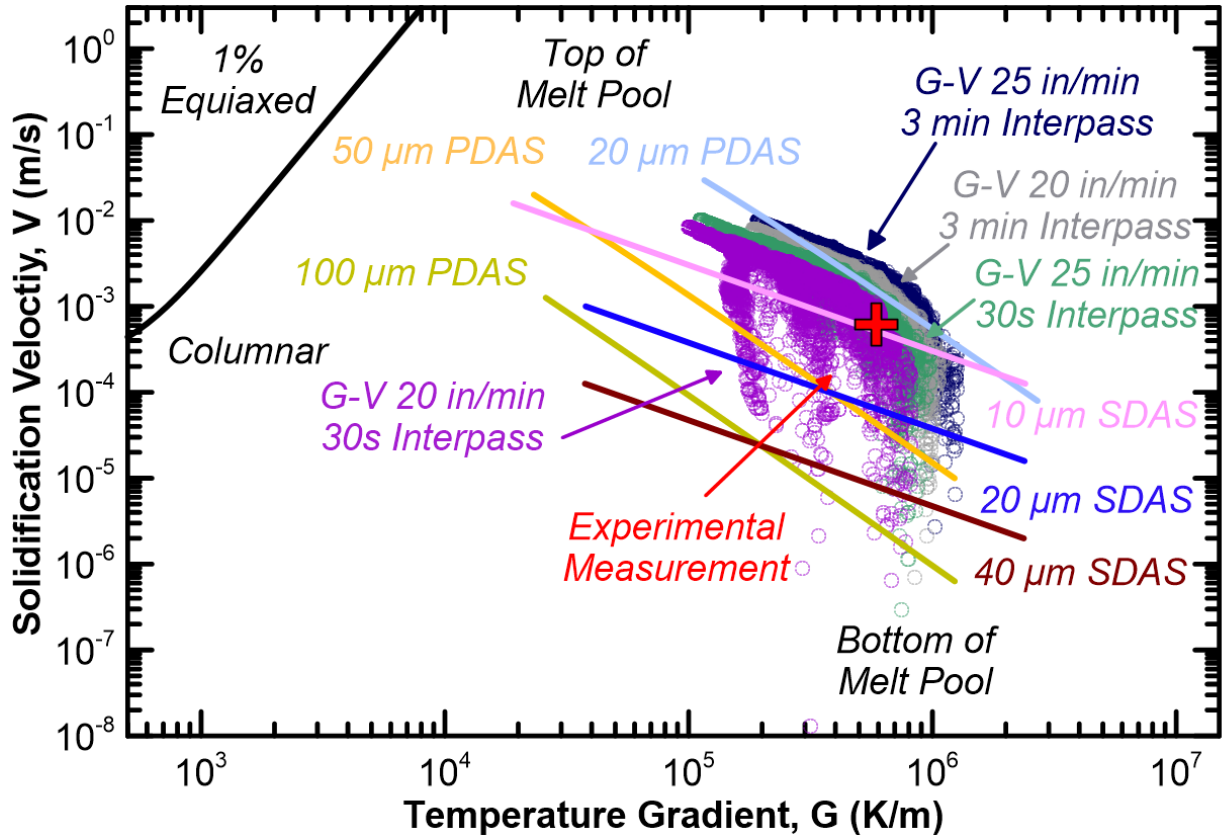

Figure 3.15 *G,V* values from heat transfer model with predicted dendrite arm spacings for 316LSi in comparison with experimentally measured dendrite arm spacings. Experimental measurement point combines both PDAS and SDAS

3.8 References

3.1 Gisario, Annamaria, et al. "Metal additive manufacturing in the commercial aviation industry: A review." Journal of Manufacturing Systems 53 (2019): 124-149.

3.2 2. Desu, Raghuram Karthik, et al. "Mechanical properties of Austenitic Stainless Steel 304L and 316L at elevated temperatures." Journal of Materials Research and Technology 5.1 (2016): 13-20

3.3 J.C. Lippold, V.F. Savage “Solidification of austenitic stainless steel weldments: Part I—a proposed mechanism” Weld. J., 58 (1979), pp. 362-374

3.4 Frazier, William E. "Metal additive manufacturing: a review." Journal of Materials Engineering and performance 23.6 (2014): 1917-1928.

3.5 DeLong, W. T. "Ferrite in austenitic stainless steel weld metal." (1974).

3.6 Brooks, J. A., and A. W. Thompson. "Microstructural development and solidification cracking susceptibility of austenitic stainless steel welds." International Materials Reviews 36.1 (1991): 16-44.

3.7 Chen, Xiaohui, et al. "Effect of heat treatment on microstructure, mechanical and corrosion properties of austenitic stainless steel 316L using arc additive manufacturing." Materials Science and Engineering: A 715 (2018): 307-314.

3.8 Inoue, Hiroshige, and Toshihiko Koseki. "Solidification mechanism of austenitic stainless steels solidified with primary ferrite." Acta Materialia 124 (2017): 430-436.

3.9 Easton, Mark, Cameron Davidson, and David St John. "Effect of alloy composition on the dendrite arm spacing of multicomponent aluminum alloys." Metallurgical and materials transactions A 41.6 (2010): 1528-1538.

3.10 “Blue Max Mig 316L.” Blue Max® MiG 316L, https://www.lincolnelectric.com/en/products/bluemaxmig316l_gmaw.

3.11 ASTM E8/E8M-22. "Standard test methods for tension testing of metallic materials." Annual book of ASTM standards. ASTM (2022).

3.12 “Lincoln® Red Max® 316lsi.” LINCOLN® Red Max® 316LSi, https://www.lincolnelectric.com/en/Products/lincolnredmax316lsi_gmaw?sku=ED036768.’

3.13 Cunningham, C. R., et al. "Effects of in-process LN2 cooling on the microstructure and mechanical properties of type 316L stainless steel produced by wire arc directed energy deposition." Materials Letters 282 (2021): 128707.

3.14 ASME 1998 Section II, AMSE SA-240/SA-240M,Specification for Heat-Resisting Chromium and Chromium-Nickel Stainless Steel Plate, Sheet, and Strip for Pressure Vessels, ASME, New York, NY, 1998, pp. 363–70.i.

3.15 ISO, EN. "2566-1." Steel — Conversion of elongation values — Part 1: Carbon and low-alloy steels” ISO (2021).

3.16 Chao, Qi, et al. "The effect of post-processing heat treatment on the microstructure, residual stress and mechanical properties of selective laser melted 316L stainless steel." Materials Science and Engineering: A 821 (2021): 141611.

3.17 Cunningham, C. R., et al. "Characterisation of Austenitic 316 LSi Stainless Steel Produced by Wire Arc Additive Manufacturing with Interlayer Cooling." 2019 International Solid Freeform Fabrication Symposium. University of Texas at Austin, 2019.’

3.18 Wu, Amanda S., et al. "An experimental investigation into additive manufacturing-induced residual stresses in 316L stainless steel." Metallurgical and Materials Transactions A 45.13 (2014): 6260-6270.

3.19 Rosli, Nor Ana, et al. "Review on effect of heat input for wire arc additive manufacturing process." journal of materials research and technology 11 (2021): 2127-2145.

3.20 Elmer, J. W., S. M. Allen, and T. W. Eagar. "Microstructural development during solidification of stainless steel alloys." Metallurgical transactions A 20.10 (1989): 2117-2131.

3.21 Gäumann, M., et al. "Single-crystal laser deposition of superalloys: processing–microstructure maps." Acta materialia 49.6 (2001): 1051-1062.

3.22 Kurz, W. 1., B. Giovanola, and R. Trivedi. "Theory of microstructural development during rapid solidification." Acta metallurgica 34.5 (1986): 823-830.

3.23 Yonezawa, Toshio, et al. "The effect of chemical composition and heat treatment conditions on stacking fault energy for Fe-Cr-Ni austenitic stainless steel." Metallurgical and Materials Transactions A 44.13 (2013): 5884-5896.

3.24 Jeong, Kookhyun, et al. "The effects of Si on the mechanical twinning and strain hardening of Fe–18Mn–0.6 C twinning-induced plasticity steel." Acta Materialia 61.9 (2013): 3399-3410.

3.25 Eliasson, Johan, and Rolf Sandström. "Proof strength values for austenitic stainless steels at elevated temperatures." Steel research 71.6-7 (2000): 249-254.

3.26 Dantzig, Jonathan A., and Michel Rappaz. Solidification: -Revised & Expanded. EPFL press, 2016.

3.27 Paskual, Amagoia, Pedro Álvarez, and Alfredo Suárez. "Study on arc welding processes for high deposition rate additive manufacturing." Procedia Cirp 68 (2018): 358-362.

3.28 Williams, Stewart W., et al. "Wire+ arc additive manufacturing." Materials science and technology 32.7 (2016): 641-647.

3.29 Lipton, J., M. E. Glicksman, and W. Kurz. "Dendritic growth into undercooled alloy metals." Materials Science and Engineering 65.1 (1984): 57-63.

3.30 Lipton, J., M. E. Glicksman, and W. Kurz. "Equiaxed dendrite growth in alloys at small supercooling." Metallurgical and Materials Transactions A 18.2 (1987): 341-345.

3.31 Gäumann, M., R. Trivedi, and W. Kurz. "Nucleation ahead of the advancing interface in directional solidification." Materials Science and Engineering: A 226 (1997): 763-769.

3.32 Poling, Whitney. Grain size effects in micro-tensile testing of austenitic stainless steel. Colorado School of Mines, 2012.

3.33 Sherby, Oleg D., and Eric M. Taleff. "Influence of grain size, solute atoms and second-phase particles on creep behavior of polycrystalline solids." Materials Science and Engineering: A 322.1-2 (2002): 89-99.

3.34 Valiorgue, Frédéric, et al. "Emissivity calibration for temperatures measurement using thermography in the context of machining." Applied Thermal Engineering 58.1-2 (2013): 321-326.

3.35 Vander Voort, George F., et al. "ASM handbook." Metallography and microstructures 9 (2004): 44073-0002.

3.36 Small, Katharine B., David A. Englehart, and Todd A. Christman. "Etching specialty alloys." Advanced materials & processes (2008): 33.

3.37 Peter Pichler , Brian J. Simonds, Jeffrey W. Sowards, and Gernot Pottlacher (2020) Measurements of thermophysical properties of solid and liquid NIST SRM 316L stainless steel. Mater Sci (2020) 55:4081–4093

3.38 British Stainless Steel Association, https://bssa.org.uk/bssa_articles/elevated-temperature-physical-properties-of-stainless-steels/, accessed on 10 October 2020

3.39 Hiroyuki Fukuyama, Hideo Higashi & Hidemasa Yamano (2019) Thermophysical Properties of Molten Stainless Steel Containing 5 mass % B4C, Nuclear Technology, 205:9, 1154-1163, DOI: 10.1080/00295450.2019.1578572

3.40 John A. Goldak, Mehdi Akhlaghi (2005) COMPUTATIONAL WELDING MECHANICS. Springer. https://link.springer.com/book/10.1007%2Fb101137

CHAPTER 4

LACK OF FUSION DEFECTS IN WA-DED OF 316L

Lack of Fusion defects in WA-DED 316L and 316LSi were studied by introducing controlled defects within representative builds. A high deposition rate pulsed spray weld mode was used to construct builds with increasing hatch spacing to induce lack of fusion defects. Using a thermal camera system, formation of lack of fusion was successfully observed during deposition, and a bead width to hatch spacing ratio at which WA-DED 316L and 316LSi become susceptible to lack of fusion was established.

4.1 Introduction

Wire-arc directed energy deposition (WA-DED), also known as wire arc additive manufacturing (WAAM), is being studied as a potential manufacturing method to produce valve bodies for use within power plants. A key advantages of using WA-DED for this application is lowering the lead time for replacement parts [4.1]. However, a greater understanding of the WA-DED process must be developed before it can be used for this application, this study aims to examine lack of fusion defects within high deposition rate WA-DED of 316L.

Defects within parts fabricated with WA-DED can be a result of multiple factors, including contamination, high residual stresses, unstable weld processes, and poor tool-path selection [4.6]. Lack of fusion (LOF) defects arise from a failure of the weld bead to fuse to the base material, previous layers, or neighboring weld beads. This can be caused by insufficient heat input, incorrect tool path, or too great of travel speed [4.2]. In laser powder bed fusion (LPBF) lack of fusion comes about from neighboring melt pools having limited overlap, resulting in undesirable porosity [4.3].

Previous work has been performed to study the impact of gas pore on WA-DED. Romali *et al*. by constructing WA-DED build with contaminated Ti-6Al-4V wire feedstock were successfully able induce pores over 100 μm in diameter, showing a reduction in density from 99.9% in the control build to 99.6% in the contaminated build. They show that the builds have comparable yield strength and tensile strength, but that the contaminated samples display a lower elongation [4.7].

While work has been done to study the impacts of small gas pores, limited work has been done to study lack of fusion defects within WA-DED and their impact on mechanical properties. This study aims to evaluate the impact on mechanical properties of lack of fusion defects on WA-DED 316L by inducing controlled lack of fusion defects within representative WA-DED 316L builds. Lack of fusion is introduced into representative builds by increasing the distance between parallel weld beads. Defect formation is observed in-situ through a thermal camera.

4.2 Experimental Methods

To construct builds, a THG Automation collaborative robot system was used, which packages together a Universal Robots UR10e collaborative robot with a Fronius CMT power source. A pulsed spray weld mode was utilized with a wire feed rate of 10.16 m/min (400 in/min) with 1.14 mm (0.045 in) diameter wire, resulting in a deposition rate of 5 kg/hr. A 95% Ar + 5% CO_2 shielding gas was used with a flow rate of approximately 25 CFH. A travel speed of 16.9 mm/s or 40 in/min was used. Builds were constructed with both Lincoln Electric Blue Max® MIG 316L wire and using Lincoln Electric Red Max® MIG 316LSi wire, the composition of which can be seen in Table 1. Builds measuring 127 mm x 102 mm x 51 mm (5 in x 4 in x 2 in) were constructed using a parallel bead tool path. After construction, all builds were heat treated at 1040 °C for one hour a using Carbolite CWF 13/5 and water quenched.

Table 4.1 Typical wire composition of Lincoln Electric Blue Max® MIG 316L [4.4] and Lincoln Electric Red Max® MIG 316LSi [4.5]

	%C	%Cr	%Cu	%Mn	%Mo	%N	%Nb	%Ni	%P	%S	%Si
Lincoln Electric Blue Max® MIG 316L	0.01 -0.02	18.5 -18.7	0.03 -0.13	1.6 - 1.8	2.1 - 2.6	0.03	0.01 max.	11.8 - 12.2	0.02	0.01 max	0.39 - 0.40
Lincoln Electric Red Max® MIG 316LSi	0.01-0.02	18.2-18.3	0.07-0.10	1.7	2.3	0.06 - 0.07	0.01 max.	11.3	0.02	0.02	0.79 – 0.87

Bead or hatch spacing was selected by performing single layer builds with varying spacing using the weld parameters outlined above. The hatch spacing that resulted in a defect free single layer build was selected as the baseline, and then bead spacing was increased by 0.5 mm and 1 mm from this baseline. This process was done for both 316L and 316LSi wire filler metal. Additionally, bead width was measured for both materials to calculate the bead width to hatch spacing ratio. The bead spacing, bead width, and hatch spacing to bead width ratio are summarized in Table 2.

Table 4.2 Build spacing parameters used for defect builds.

Build	Material	Bead Width (mm)	Hatch Spacing (mm)	Hatch Spacing to Bead Width Ratio
1	316L	5.1	3.0	0.58
2	316L	5.1	3.5	0.68
3	316L	5.1	4.0	0.78
4	316LSi	5.6	3.5	0.63
5	316LSi	5.6	4.0	0.71
6	316LSi	5.6	4.5	0.80

The toolpath for the collaborative robot system was generated using the open-source software Cura, a CAD model of build was created and imported into Cura as a STL file. A toolpath of parallel beads was used, as shown in Figure 4.1, with the travel direction alternating

each layer. Within Cura, bead width was set to the desired hatch spacing for each build, and layer height was set to match the weld bead height. Travel speed was set to 16.9 mm/s (40 in/min).

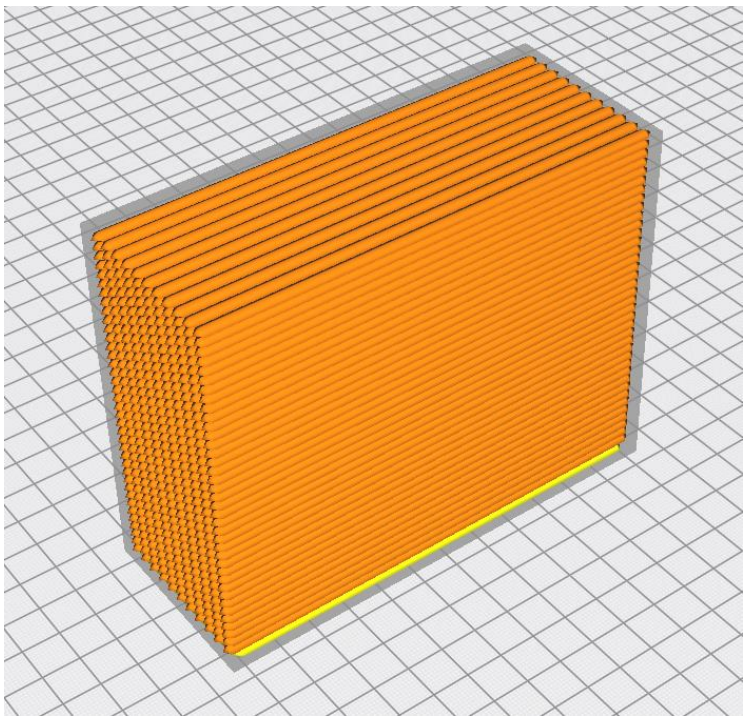

Figure 4.1 Toolpath used for defect build construction.

A Xiris XIR-1800 short wavelength infrared thermal camera was used to observe the build process and confirm the formation of LOF defects during deposition of the 316LSi 4.5 mm build and the 316LSi 3.5 mm build. Video was captured over the deposition of two successive layers.

4.3 Results and Discussion

Single layer depositions were performed for a variety of bead spacing's in 0.5 mm increments. Once a defect free bead spacing was found, bead spacing was increased by 0.5 mm and 1 mm from this baseline. Figure 4.2 shows the evolution of defects as bead spacing increases. In the tightest bead spacing for both 316L and 316LSi no defects are observed, at 0.5

mm above this baseline a limited number of defects begin to appear, and at 1 mm above the baseline a large amount of LOF defects are observed. These results show that at a hatch spacing to bead width ratio of approximately 0.7 WA-DED of 316L and 316LSi begin to become susceptible to LOF, and at ratio's nearing 0.8 LOF becomes more prevalent. This visual inspection however, does not discount the possibility of subsurface LOF.

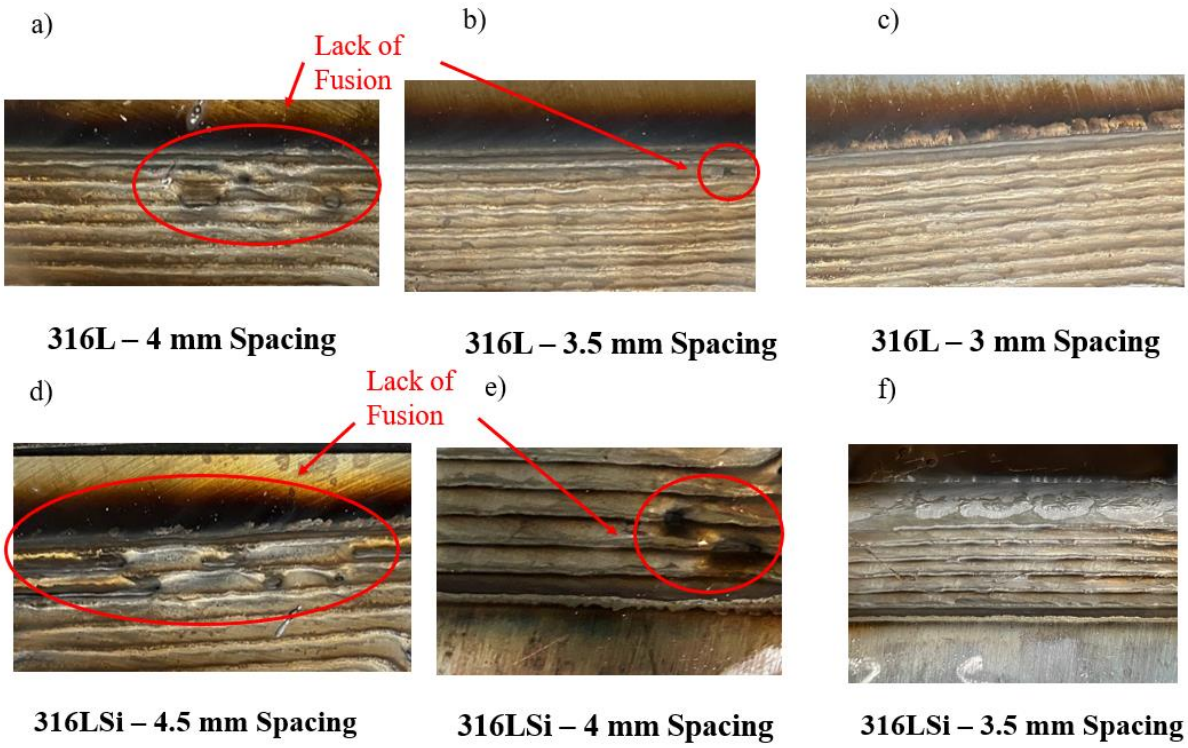

Figure 4.2 Single layer depositions used to determine bead spacing for small scale defect builds.

Figure 4.3 show images captured with a Xiris XIR-1800 short wavelength infrared thermal camera during production of the 316LSi 4.5 mm spacing build and the 316LSi 3.5 mm spacing build. In the 316LSi 3.5 mm condition (Figure 4.3b) no LOF defects are observed, whereas in the 316LSi 4.5 mm condition multiple LOF defects can be seen (Figure 4.3a). Additionally, video was captured for two successive layers and the LOF of fusion defects seen in

Figure 4.2 do not appear to fully fill in when the next layer is deposited over the defects, further indicating that the LOF defects remain in the completed build.

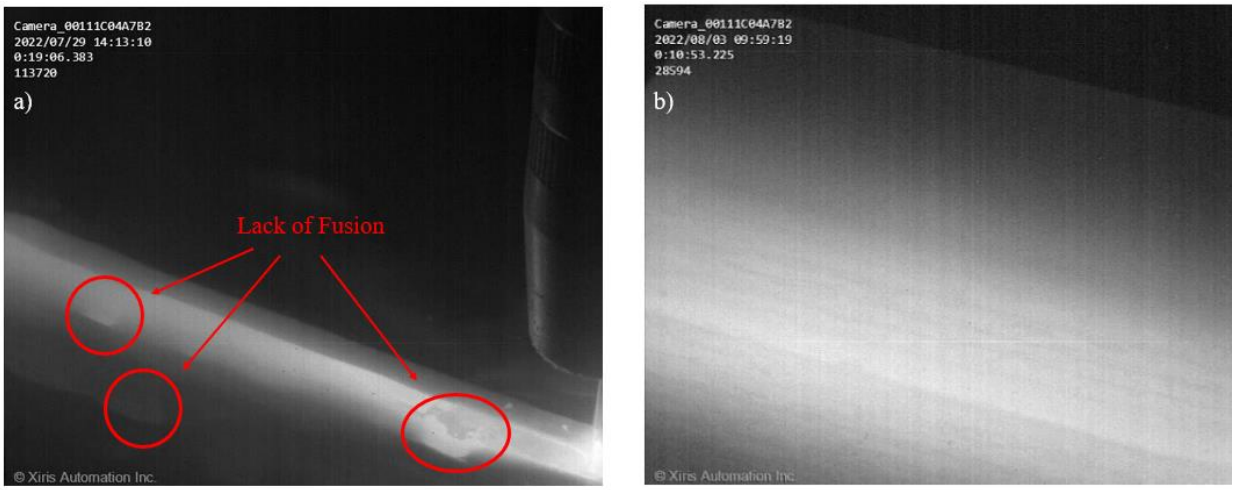

Figure 4.3 In-site images of a) 316LSi – 4.5 mm spacing build showing LOF and b) 316LSi – 3.5 mm spacing showing no defects.

Bead width can be impacted by multiple factors. 316LSi displays a wider bead over 316L with identical process parameters and conditions. Si addition has been previously shown to reduce the surface tension of the melt pool, leading to the wider melt pool observed with 316LSi filler metal [4.8]. Additionally, the addition of CO_2 to Ar in the shielding gas reduces the surface tension of the molten weld bead during deposition, also resulting in a wider weld bead [4.9]. Therefore, changes in feedstock composition and shielding gas can have significant impacts on the formation of lack of fusion defects in WA-DED. However, differences in the likelihood of lack of fusion formation can be estimated based on changes of various process parameters on bead width, and hatch spacings can be adjusted accordingly.

From these results, based on thermography and visual inspection, WA-DED of 316L and 316LSi likely becomes susceptible to LOF at hatch spacing to bead width ratios greater than

0.68, with a large amount of LOF being observed in-situ at a ratio of 0.8. These criteria can be used to design deposition strategies for WA-DED builds while eliminating lack of fusion porosity.

4.4 Conclusions

Lack of fusion defects were induced in representative WA-DED builds through altering hatch spacing relative to the bead with 316L and 316LSi feedstocks while monitoring the deposition process with an infrared camera. From these results, the following conclusions are made:

- Lack of fusion defects appear in WA-DED builds when a critical value of hatch spacing to bead width is reached. Hatch spacing to bead width ratios was used to evaluate at what point WA-DED 316L and 316LSi become susceptible to LOF defects, with LOF being observed with thermography a 316LSi build with a 0.8 ratio. To minimize the possibility of LOF, it is recommended that the bead width to hatch spacing ratio be maintained bellow 0.68.
- An infrared thermal camera was able to detect when lack of fusion occurred in the build process, suggesting that thermography is a viable tool for in-process monitoring and control.

Further work is actively being undertaken to evaluate the impact on mechanical properties of LOF defects.

4.5 References

4.1 Gisario, Annamaria, et al. "Metal additive manufacturing in the commercial aviation industry: A review." Journal of Manufacturing Systems 53 (2019): 124-149

4.2 Loppold, John C. *Welding metallurgy and weldability*. John Wiley & Sons, 2014.

4.3 Tang, Ming, P. Chris Pistorius, and Jack L. Beuth. "Prediction of lack-of-fusion porosity for powder bed fusion." Additive Manufacturing 14 (2017): 39-48.

4.4 “Blue Max Mig 316L.” Blue Max® MiG 316L, https://www.lincolnelectric.com/en/products/bluemaxmig316l_gmaw.

4.5 “Lincoln® Red Max® 316lsi.” LINCOLN® Red Max® 316LSi, https://www.lincolnelectric.com/en/Products/lincolnredmax316lsi_gmaw?sku=ED036768.’

4.6 Wu, Bintao, et al. "A review of the wire arc additive manufacturing of metals: properties, defects and quality improvement." Journal of Manufacturing Processes 35 (2018): 127-139.

4.7 Biswal, Romali, et al. "Criticality of porosity defects on the fatigue performance of wire+ arc additive manufactured titanium alloy." International Journal of Fatigue 122 (2019): 208-217.

4.8 Pollard, B. "The effects of minor elements on the welding characteristics of stainless steel." Welding Journal 67.9 (1988): 202s-213s.

4.9 Subramaniam, S., and D. R. White. "Effect of shield gas composition on surface tension of steel droplets in a gas-metal-arc welding arc." Metallurgical and materials transactions B 32.2 (2001): 313-318.

CHAPTER 5

LARGE-SCALE WA-DED 316L BODY GENERATION

In collaboration with Oak Ridge National Lab Manufacturing Demonstration Facility (ORNL MDF) a large scale, representative WA-DED 316L valve body was produced. This chapter discusses this process, including print strategy, part design, and tool path generation.

5.1 Part Design and Print Strategy For WA-DED

A large-scale, representative valve body, shown in Figure 5.1, was to be produced through WA-DED of 316L. An initial CAD model was provided by Electric Power Research Institute (EPRI), but multiple changes were made to optimize the part for WA-DED production. However, before making any changes to the part design, a print strategy was developed.

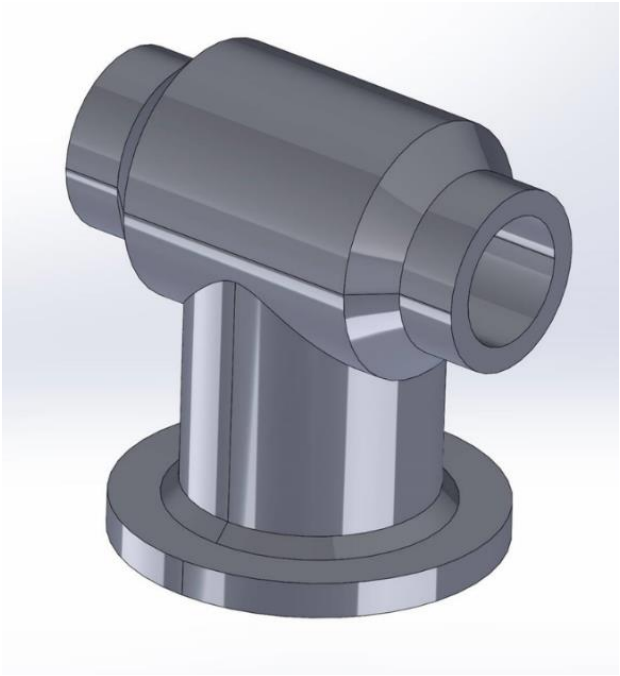

Figure 5.1 Original model of valve body to be produced through WA-DED.

The ORNL MDF WA-DED system consists of a six-axis robot arm as well as a positioner table, allowing for changing the part orientation and position during printing and providing more freedom when developing a print strategy. Considering the full capability of the ORNL equipment, a print strategy was developed where the component would be split into three print stages, shown in Figure 5.2, consisting of the top tube section, the base tube section, and the flange section.

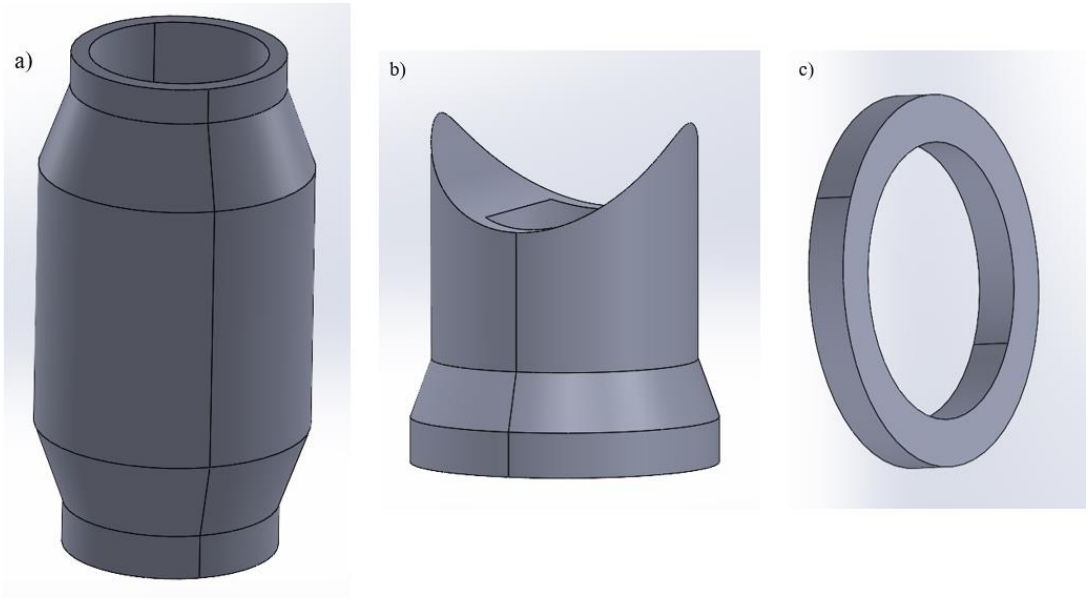

Figure 5.2 Three separate print stages developed from original model showing a) the top tube section, b) the base tube section, and c) the flange section.

With the initial model split into three sections, a print strategy was developed where the top tube section would be printed vertically first, the positioner table would then be rotated, and the base tube would be printed vertically off the now horizontal top tube. Due to the cylindrical shape of these sections, it was decided that these sections would be printed using a cylindrically infill tool path. With the two tube sections printed, the part was once again rotated using the positioner table system so that the base tube section would be oriented horizontally. For the

flange section, a print strategy was developed where the robot and weld torch would remain vertical, and the positioner table would be rotated to print the flange section around the base tube. This type of print strategy is only possible because of the positioner table in ORNL MDF WA-DED system. After the print strategy was developed, the part design was modified to be more conducive to the printing process.

The first part design changes made were to account for necessary overbuilding as well as to update wall thickness to match bead size. Due to the rough surface finish associated with the WA-DED process, overbuilding is necessary so that rough surfaces can be machined while still maintaining minimum thicknesses. To account for this, the thickness of all surfaces was increased by 6.35 mm. Additionally, wall thickness was increased to be an integer of bead width, approximately 4.2 mm, to allow for simplified toolpath generation. Further, the maximum overhang that can be built with 316L on this system is roughly 20°, so all overhangs within the CAD model were reduced to be no greater than this value. These changes can be seen in Figure 5.3 on page 63.

One final update was made to CAD model to simplify the printing process. A flat portion was added to the top tube section to create surface to print the bottom tube section from. Additionally, the top of the base tube section was flattened to allow for this section to be printed from the update top tube part. With these final updates, the completed CAD models, shown in Figure 5.4 on page 64, were ready for toolpath generation before WA-DED production.

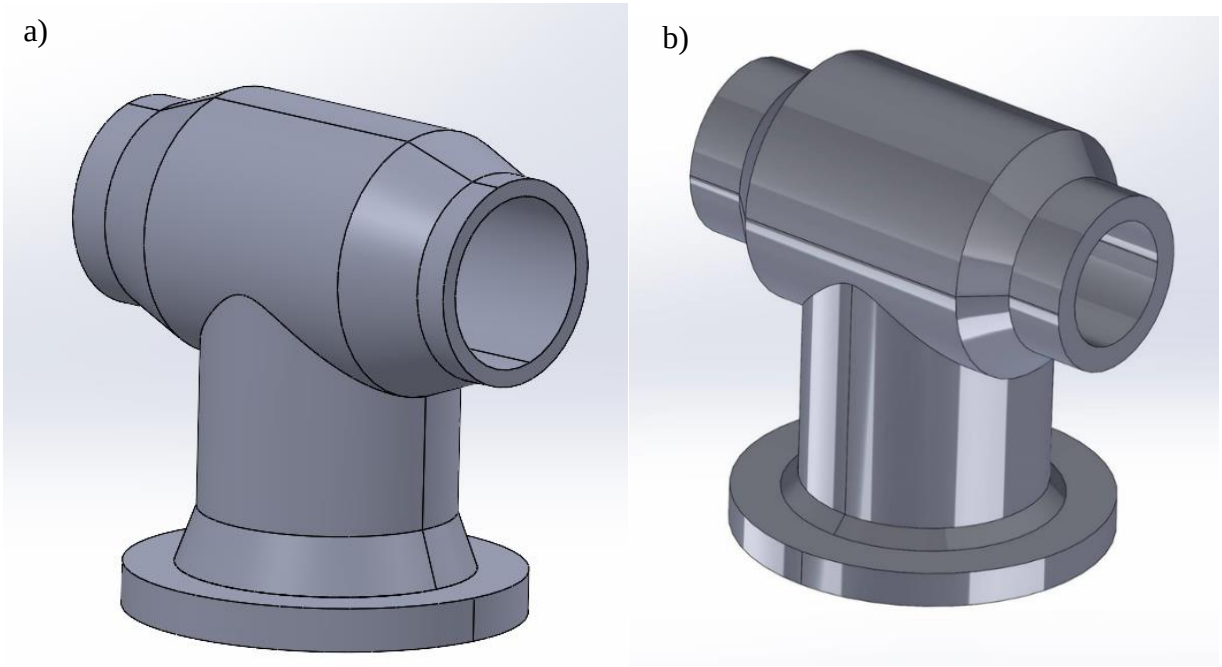

Figure 5.3 a) CAD model of valve body for WA-DED after modifying for overbuilding and overhangs. b) Original model of valve body.

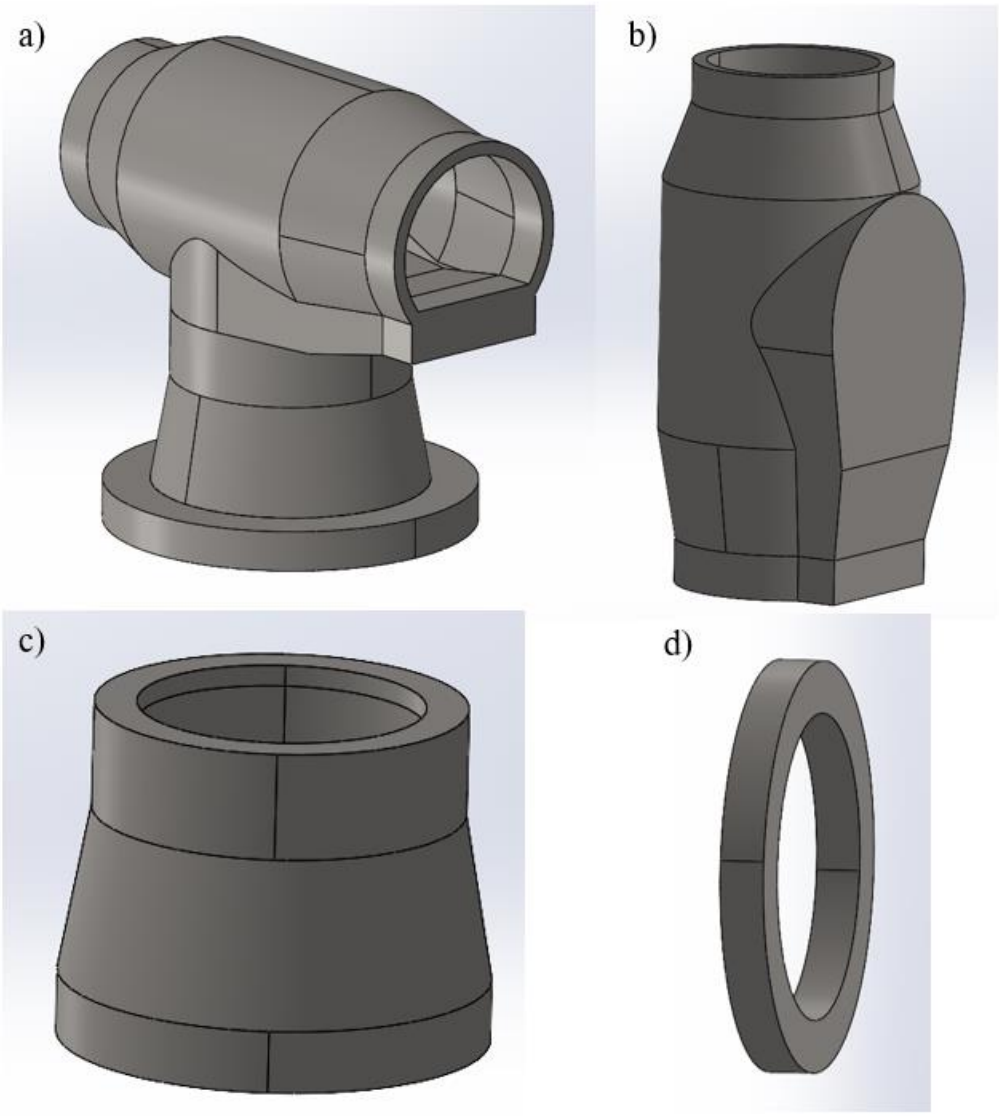

Figure 5.4 Completed CAD models for large-scale WA-DED 316L body, showing a) the entire valve body model, b) the top tube section, c) the base tube section, and d) the flange section.

5.2 Toolpath Generation

The toolpath G-code for producing the large-scale valve body with the ORNL MDF WA-DED system was generated using a proprietary slicing software similar to the open-source software, Cura.

To generate G-code, CAD models were first imported into Cura as STL files and oriented in the build direction and centered on the build plane, as shown in Figure 5.5. Within Cura, a few key settings were updated. Firstly, layer height and width within Cura was set to match that of the weld bead geometry, approximately 2.1 mm and 4.2 mm respectively. Additionally, infill style was set to concentric and travel speed was set to match the desired print speed, 16.93 mm/s. Infill paths were also connected to minimize weld start and stop events. With these setting updated, the part could then be sliced and the G-code generated, as shown in Figure 5.5. Following this same process, G-code was generated for all three build sections. G-code could then be imported into the WA-DED system to produce the large-scale build.

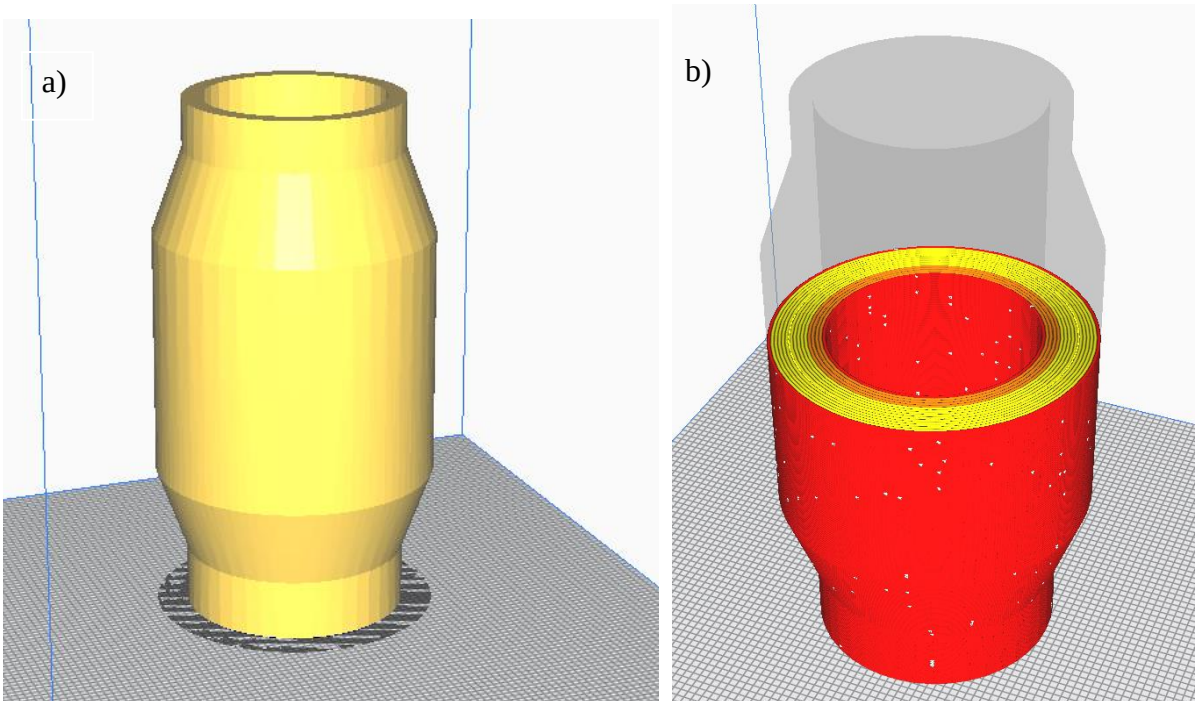

Figure 5.5 a) CAD model of top tube section of valve-body imported into Cura and oriented with the build direction. b) Top tube section of valve body after G-code generation in Cura, showing tool path and concentric infill.

5.3 Large-Scale Valve Body Production With WA-DED

Once G-code was generated, the valve-body could be produced using the ORNL MDF WA-DED system. This system incorporates a Lincoln Electric gas metal arc welding (GMAW) power source, and for this build, the Rapid X™ pulsed spray weld mode was used, with a wire feed rate of 10.16 m/min (400 in/min). Lincoln Electric Blue Max® MIG 316L with a 1.14 mm (0.045 in) diameter was used as the wire feedstock and a 95% Ar + 5% CO2 shielding gas with a flow rate of 25 CFH was used during deposition.

The build process was performed by the ORNL MDF team following the print strategy outlined in section 5.1. Figure 5.6 shows the completed build of the valve-body. The final build took approximately 12 hours, with the top tube section measuring approximately 323 mm (12.7 in) tall. This build process demonstrated the importance of build strategy and part design for successful WA-DED builds and showed that WA-DED can be used to successfully produce these large-scale valve bodies.

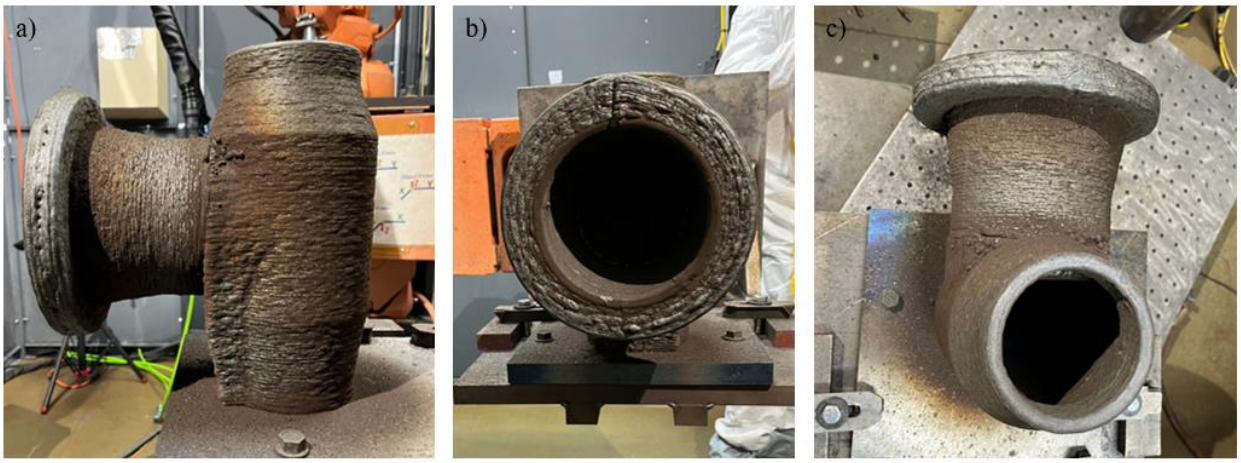

Figure 5.6 Completed large-scale WA-DED 316L valve body as seen from a) side view, b) the flange section, and c) the top view.

CHAPTER 6

CONCLUSIONS AND FUTURE WORK

WA-DED of 316L was examined through parametric exploration, development of microstructure prediction models, examination of process induced lack of fusion defects, and generation of a large-scale body. A general summary of the work performed is presented here to respond to the research questions posed in Chapter 1. Additionally, this chapter presents recommendations for future work.

6.1 Conclusions

Question 1: What are the effects of travel speed, interpass temperature, and silicon content on the tensile properties of WA-DED 316L?

- All samples heat treated at 1040 °C for 1 hour and water quenched met ASME minimums of a yield strength of 172 MPa, a tensile strength of 482 MPa, and an elongation of 43.6% in one inch for 316L at room temperature. Samples in the as-built condition displayed a higher strength than heat treated samples, but failed to meet ASME minimums for ductility.
- Interpass temperature and travel speed were shown to have a minimal effect on mechanical properties of WA-DED 316L within the ranges evaluated.
- Samples constructed with 316LSi displayed a higher yield strength, ultimate tensile strength, and ductility compared to samples constructed with 316L. The increase in strength is associated with solid solution strengthening from the added silicon and nitrogen, and the increase in ductility is associated with a reduction in stacking fault energy from added silicon and reduced nickel.

- Sampled met the ASME minimum for yields strength at 427 °C (800 °F) of 99 MPa, but failed to meet the ASME minimum for tensile strength at 427 °C (800 °F) of 417 MPa. The measured tensile strengths are possibly lower than expected due to the large grain size relative to the tensile specimen size affecting the amount of strain hardening, but further testing is needed.

Question 2: Can a heat transfer model, in conjunction with solidification models, be used to predict the as-built microstructure of WA-DED 316L?

- A heat transfer model was developed to predict the thermal history of the WA-DED process. This model was combined with dendrite spacing and microstructure morphology models to make microstructure predictions. Experimental measurements from the as-built microstructure of show primarily columnar dendrites with a PDAS values of 22.3 – 25.9 µm and a SDAS of 8.0 – 9.1, agreeing with model predictions, indicating the possibility for modelling to be used to assist in process optimization.

Question 3: What is the critical hatch spacing between passes to generate lack of fusion porosity, and can porosity be detected in-process?

- To establish a critical point for lack of fusion, hatch spacing to bead width ratio was used. In bead on plate studies, lack of fusion began to appear at a ratio of approximately 0.7, and lack of fusion during the WA-DED process was observed with thermography at a ratio of approximately 0.8. To minimize the possibility of LOF, it is recommended that a bead width to hatch spacing ratio be maintained bellow 0.68.
- Lack of fusion was detected with an infrared camera suggesting that this tool can be used for in-process monitoring and control in the WA-DED process.

Question 4: What considerations must be made when designing parts to be made by WA-DED?

- Part design and optimization for WA-DED is driven by the print strategy. For complex parts the build process can be simplified by printing the part in separate stages.
- To allow for post process machining, an overbuilding of approximately 6.5 mm in recommended.
- These strategies were used to successfully produce a large-scale WA-DED 316L body.

6.2 Future Work

Multiple future research pathways are presented here based on the work and results described in this project.

- To confirm the tensile strength properties of WA-DED 316L, it is recommended that further tensile testing be performed with larger tensile specimens in order to capture more grains within tensile samples.
- Creep, fatigue, and toughness testing is recommended to further evaluate the mechanical performance of WA-DED 316L. Good creep performance is expected as the large grains associated with the WA-DED process minimize the potential for grain boundary sliding.
- In this study, silicon and nitrogen were shown to act as a potent strengthener while simultaneously increasing ductility. Evaluation of other alloying addition to 316L presents a pathway for future work.
- Tensile testing is actively being pursued to better understand how process defects impact the mechanical properties of WA-DED 316L produced samples. This would allow for additional support to establish a critical bead width to hatch spacing ratio.

- Evaluation of the mechanical properties of the large-scale body allows for comparison to the research done on small-scale builds presented in this work, and to confirm that properties of WA-DED 316L stay consistent throughout varying size scales.